The Astrophysical Journal, 570:825–854, 2002 May 10

PENETRATION AND OVERSHOOTING IN TURBULENT COMPRESSIBLE CONVECTION

Nicholas H. Brummell, Thomas L. Clune, and Juri Toomre
JILA and Department of Astrophysical and Planetary Sciences, University of Colorado, Boulder, CO 80309-0440
Received 2001 August 24; accepted 2002 January 16

ABSTRACT

We present the results of a series of high-resolution, three-dimensional numerical experiments that investigate the nature of turbulent compressible convective motions extending from a convection zone into a stable layer below. In such convection, converging flows in the near-surface cellular convecting network create strong downflowing plumes that can traverse the multiple scale heights of the convection zone. Such structures can continue their downward motions beyond the convecting region, piercing the stable layer, where they are decelerated by buoyancy braking. If these motions mix entropy to an adiabatic state below the convection zone, the process is known as penetration; otherwise it is termed overshooting. We find that in three-dimensional turbulent compressible convection at the parameters studied, motions generally overshoot a significant fraction of the local pressure scale height but do not establish an adiabatic penetrative region, even at the highest Péclet numbers considered. This is mainly due to the low filling factor of the turbulent plumes. The scaling of the overshooting depth with the relative stability S of the two layers is affected by this lack of true penetration. Only an S^{-1} dependence is exhibited, reflecting the existence of a thermal adjustment region without a nearly adiabatic penetration zone. Rotation about a vertical axis decreases the depth of overshooting, owing to horizontal mixing induced by the rotation. For rotation about an inclined axis, turbulent rotational alignment of the strong downflow structures decreases the overshooting further at mid-latitudes, but the laminar effects of cellular roll solutions take over at low latitudes. Turbulent penetrative convection is quite distinct from its laminar counterpart and from the equivalent motions in a domain confined by impenetrable horizontal boundaries. Although overshooting would not be so deep in the solar case, the lack of true penetration extending the adiabatic region may explain why helioseismic inferences show little evidence of the expected abrupt change between the convection zone and the radiative interior. These results may also provide insight into how overshooting motions can provide a coupling between the solar convection zone and the tachocline.

Subject headings: convection — stars: interiors — Sun: interior — turbulence

1. INTRODUCTION

While inferences of the structure of the solar interior are becoming more precise, theoretical explanations for these observations are not as forthcoming. Helioseimology has revealed (see, e.g., Thompson et al. 1996) a differentially rotating convection zone and a solid-body rotating radiative interior, joined by a thin transition region (Goode et al. 1991) that has become known as the tachocline because of the strong gradient in angular velocity there (Spiegel 1972; Spiegel & Zahn 1992). Theoretically, the motivation for comprehending these interior dynamics is high, since it is believed that the convection zone and its differential rotation, especially the strong shear of the tachocline, must play an important role in the generation of the solar magnetic activity cycle. However, despite this intuitive understanding of the operation of the solar cycle built upon a mixture of observation and simple theory (for a review, see Weiss 1994), robust detailed theoretical explanations have not yet materialized. For example, the constant-on-radii angular velocity distribution of the convection zone deduced from helioseismology is proving difficult to reproduce in self-consistent models (Gilman 1975, 1977; Glatzmaier & Gilman 1981a, 1981b; Glatzmaier 1984, 1985a, 1985b; Gilman & Miller 1986; Miesch et al. 2000; Elliott, Miesch, & Toomre 2000), and the cause of the solid-body rotation of the radiative core has prompted much diverse speculation (Kumar & Quataert 1997; Zahn, Talon, & Matais 1997; Gough 1997; Gough & MacIntyre 1998).

The tachocline presents further problems. The structure of the layer is not clear even observationally, owing to the low resolution of the inversion kernels in helioseismic studies at that depth. Indeed, even where the convection zone ends, where the tachocline starts, and whether they in fact overlap, is not clearly apparent from the helioseismic inversions (Christensen-Dalsgaard, Gough, & Thompson 1991; Thompson et al. 1996). Not surprisingly then, theoretical modeling of the dynamics of the tachocline is at a primitive stage. Even evidently robust characteristics currently attract contradictory theories. The remarkable thinness of the tachocline, for instance, has spawned models based upon both turbulent and laminar processes either with or without magnetic fields; Spiegel & Zahn (1992) invoke anisotropic turbulent diffusion (where the turbulence may be derived either from purely hydrodynamic [Richard & Zahn 1999] or magnetic [Gilman & Fox 1997, 1999; Gilman & Dikpati 2000] instabilities of the marginally stable shear profile [Watson 1981]), whereas Gough & MacIntyre (1998) balance laminar meridional circulations with fossil core magnetic fields. It is fair therefore to say that while the dynamics of the tachocline are considered crucial, they are currently unknown in any detail, both observationally and theoretically. The tachocline dynamically is most likely not a single layer but rather a number of sublayers, with some containing the strong toroidal magnetic field related to the activity cycle, others being mainly hydrodynamic, and deeper layers possibly being magnetohydrodynamic boundary layers to the radiative interior. The uppermost layers of the tacho-

cline must be influenced by their connection to the solar convection zone above, but the degree of this coupling is also not well understood. It is an important issue, however, since these interactions may affect the mixing and transport mechanisms for angular momentum, chemical species, and magnetic fields at the base of the convection zone, and may influence the nature of circulations and the instabilities present in the tachocline layers. This paper and related papers (e.g., Tobias et al. 2001) seek to elucidate the coupling of the convection zone with the stable layers below and therefore to address some of these issues.

The interaction between convectively unstable and stable regions has a long history of interest since there are many common natural instances where such an interface occurs: for example, when ice forms on the surface of a body of water (Malkus 1960; Furumoto & Rooth 1961; Townsend 1964; Myrup et al. 1970; Adrian 1975), or the daily transition from the nocturnal planetary boundary layer here on Earth (see, e.g., Deardorff, Willis, & Lilley 1969). It has long been understood that in convection where no impermeable boundaries are present, motions can continue beyond the region of convective driving into the surrounding stable regions. Two such types of motion are identified. First, the mixing action of such motions may alter the background state and actually extend the original (linearly unstable) region of driving. This type of extended motions is technically known as penetration. Second, motions may continue into the surrounding stable regions by inertia, even though their driving has been turned off, in a process referred to as overshooting. For many of the situations of interest, the initial background state is not known, so that any penetration that has occurred cannot be identified clearly and all that can be detected is the overshooting from the current background thermodynamics. In such cases, the terms overshooting and penetration are often used interchangeably. Indeed, in the solar case, the bottom of the convection zone is defined as the lower end of the well-mixed adiabatic region, and so any penetration in the true sense is already included as part of the convection zone.

The linear theory of penetrative convection predicts only weak unrealistic overshooting since the nonlinear feedback on the thermal stratification is missing (Veronis 1963). Veronis (and Sparrow, Goldstein, & Jonsson 1963) further performed a finite amplitude analysis of penetrative convection and discovered that the bifurcation could be subcritical. This work then led to many further nonlinear models. Models based on modal expansions arose first, providing stationary solutions for both Boussinesq fluids (Musman 1968; Moore & Weiss 1973; Zahn et al. 1982) and then a compressible (or anelastic) medium (Toomre, Gough & Spiegel 1977; Latour, Toomre, & Zahn 1981; Toomre et al. 1982; Massaguer & Zahn, 1980; Massaguer et al. 1984). All of these confirmed that nonlinear penetration was substantially deeper than linear theory predicted, indeed comparable to the depth of the unstable layer. They also gave some insight into its dependence on the parameters, in particular the stability of the outer regions and the aspect ratio of the modal planforms. The canonical low-order approach of astrophysics, that of mixing length theory, was also attempted in parallel, but such efforts proved unreliable, since the results vary drastically depending on the nonlocal formulation (see Renzini 1987 for a summary). Other simple approaches were also tried (e.g., van Ballegooijen 1982; Xiong 1985; Kuhfuss 1986), but of particular note is that of Schmitt, Rosner, & Bohn (1984), who employed the notion that the penetration occurred in the form of downward-plunging plumes. A formula was derived for the extent of penetration in terms of the exit velocity of the plumes from the convective region and their filling factor, and again it was concluded that the penetration is of the order of a pressure scale height. The constraints of the stationary modal solutions were lifted with two-dimensional studies of time-dependent fully nonlinear compressible penetration (Hurlburt et al. 1986, 1994; Roxburgh & Simmons 1993). The direct simulations of Hurlburt and coworkers showed vigorous penetration in large, overturning rolls with strong downdrafts, coupled to gravity waves in the stable layer. The latter paper (Hurlburt et al. 1994) compared further two-dimensional simulations with the analytical models of the penetration by Zahn with favorable results.

Most of the work mentioned so far has been highly simplified compared to the solar context. A number of factors must minimally be included in convection models for the dynamics to be at all truly relevant to the solar problem. Most importantly, the models must resolve as turbulent a regime as is possible, since the Sun operates at enormous Reynolds number ($\mathrm{Re} > 10^{12}$; see, e.g., Priest 1982). While the Sun also includes many other complicating effects, such as changes in the equation of state and opacities due to ionization, radiative transfer, and the presence of magnetic fields, perhaps the next most desirable property to include in the turbulent models is the asymmetry of motions induced by compressibility. Furthermore, we would like to relax the constraint of two-dimensionality and study the fully three-dimensional problem. The only tractable modeling approach incorporating these requirements is that of numerical simulation. The optimal numerical solution would compute in a global geometry representing the full star. Such approaches have yielded fundamental knowledge about the solar interior in the past (Gilman 1975, 1977; Glatzmaier & Gilman 1981a, 1981b; Glatzmaier 1984, 1985a, 1985b; Gilman & Miller 1986) and are being pursued further today (Miesch et al. 2000; Elliott et al. 2000). However, this approach suffers since the computational degrees of freedom must necessarily be assigned to the largest scales, either leaving many smaller scales unresolved or constraining the Reynolds number to be small.

Local models, where a small three-dimensional subsection of the domain is extracted and computed, lack the correct geometry but can then apply the available numerical degrees of freedom to resolving the dynamical scales from the diffusive scale up to that of the small local domain. Such simulations therefore provide a unique window into higher Reynolds number dynamics. Many such models have worked with boundary conditions traditionally reflecting the impenetrable containers used in the laboratory or the simple boundary conditions accessible to linear theory. Indeed, local models of compressible convection of this type abound and have provided significant insight (e.g., Graham 1975, 1977; Sofia & Chan 1984; Latour et al. 1981; Massaguer et al. 1984; Chan & Sofia 1986, 1987; Hurlburt et al. 1984; Cattaneo, Hurlburt, & Toomre 1989; 1990; Brandenburg et al. 1990; Malagoli, Cattaneo, & Brummell 1990; Edwards 1990; Hossain & Mullan 1990; Porter et al. 1990; Toomre et al. 1990; Cattaneo et al. 1991; Jennings et al. 1992; Nordlund et al. 1992; Pulkinnen et al. 1993; Rast & Toomre 1993a, 1993b; Bogdan, Cattaneo, & Malagoli 1994; Porter & Woodward 1994; Hurlburt et al. 1994; Matthews

1994; Toomre & Brummell 1995; Brummell, Hurlburt, & Toomre 1996; Weiss et al. 1996; Brummell et al. 1998; Tobias et al. 1998). The extension to fully turbulent, three-dimensional simulations of compressible convection in domains more related to astrophysical (and geophysical) contexts, where fluids are usually confined to a region by changing background physical conditions rather than by impenetrable containers, has not received so much attention. One series of calculations has concentrated on mimicking solar conditions as directly as possible, including the detailed physics of realistic gases and radiative transfer, with inflow and outflow lower boundary conditions (e.g., Nordlund 1982, 1983, 1984, 1985; Nordlund & Stein 1990, 1991; Stein & Nordlund 1991, 1994; Stein, Nordlund, & Kuhn 1989; Rast et al. 1993). However, these models and their boundary conditions are more directed toward solar surface conditions and granulation than the deep interior.

There have been some models that have addressed three-dimensional penetrative convection directly. Early three-dimensional turbulent simulations have been reported in Julien et al. (1996a) under the Boussinesq approximation in the oceanographic context. This paper provided the first insight into a possible reduction of penetration with the inclusion of rotation, albeit in a rundown rather than self-sustained simulation. The astrophysical context has been addressed in three dimensions by Singh et al. (1994), 1995; Muthsam et al. (1995); Singh et al. (1996, 1998a, 1998b); Nordlund et al. (1992); and Saikia et al. (2000). The bulk of the work by Singh, Chan, Roxburgh, and coworkers has corroborated many the general findings of the two-dimensional simulations. However, these models are very low resolution, using a sub–grid-scale (SGS) eddy viscosity formulation rather than solving the Navier-Stokes equations, and it is therefore sometimes difficult to interpret the results. For example, it is somewhat unclear in which regime (laminar or turbulent) these models really operate, especially when the resolution is varied (e.g., Saikia et al. 2000), thereby affecting the effective Reynolds, Rayleigh, and Péclet numbers of the flow. In light of the proximity of their results to the two-dimensional simulations, and the differences from the results presented here, we suggest that the conclusions in these works relate to the laminar or mildly turbulent regime.

The current paper therefore addresses the problem of compressible penetrative convection in the turbulent regime via local model direct simulations of the full Navier-Stokes equations. The models here build upon the previous turbulent compressible convection work of Cattaneo et al. (1991) and Brummell et al. (1996, 1998), extending the local convective domain to include a convectively stable layer below. This paper is organized as follows. In § 2 the formulation of the penetrative model is explained. In § 3 measures of penetration are constructed and the degree of penetration is examined for a range of parameters in the model. In § 4 the question of the dependence of the penetration on rotational effects is addressed. In § 5 we summarize the results and discuss the consequences for the solar interior dynamics.

2. FORMULATION

2.1. *Equations, Boundary Conditions, and Parameters*

Our two-layer model of penetrative compressible convection in a rotating plane layer is based upon a model of convection in a single layer that consists of a rectilinear domain containing a fully compressible but ideal gas confined between two horizontal, impenetrable, stress-free boundaries a distance d apart. For a single layer, the Cartesian box would span $0 \le \tilde{x} \le x_m d$ and $0 \le \tilde{y} \le y_m d$ in the horizontal and $0 \le \tilde{z} \le d$ in the vertical, with the $\tilde{z}$-axis pointing downward. The upper surface is held at a fixed temperature T_0, whereas a constant temperature gradient Δ is maintained at the lower boundary. The fields are assumed to be periodic in the two horizontal directions. The specific heats c_p and c_v, shear viscosity μ (related to the dynamic viscosity $\nu = \mu/\rho$, where ρ is the density), and the gravitational acceleration g are assumed to be constant. In a layer of constant thermal conductivity K, the temperature T_p, density ρ_p, and pressure p_p can exist in hydrostatic balance in a polytropic state:

$$T_p/T_0 = (1 + \theta\tilde{z}/d)\,, \tag{1a}$$

$$\rho_p/\rho_0 = (1 + \theta\tilde{z}/d)^m\,, \tag{1b}$$

$$p_p/p_0 = (1 + \theta\tilde{z}/d)^{m+1}\,, \tag{1c}$$

where ρ_0 is the density at the upper boundary, $p_0 = (c_p - c_v)T_0\rho_0$, and $m = -1 + g/\Delta(c_p - c_v)$ is the polytropic index and $\theta = d\ \Delta/T_o$.

Our penetrative convection configuration is built out of two such layers on top of each other in an extended Cartesian domain $0 \le \tilde{z} \le z_m d$. By specifying the polytropic indices in the two layers, we effectively impose a two-layer piecewise continuous polytropic background hydrostatic stratification, where the upper layer ($0 \le \tilde{z} \le d$, layer 1) is convectively unstable and the lower layer ($d \le \tilde{z} \le z_m d$, layer 2) is stable. The relative convective stability of the two domains is measured by the parameter, S (introduced by Hurlburt et al. 1994), defined by

$$S = \frac{m_2 - m_{\rm ad}}{m_{\rm ad} - m_1}\,, \tag{2}$$

where m_i is the polytropic index of layer i and $m_{\rm ad} = 1/(\gamma - 1)$ is the polytropic index of the adiabatic polytrope (and $\gamma = c_p/c_v$ is the ratio of the specific heats). Larger values of S correspond to an increased relative stability of the lower layer. We will sometimes refer to the relative stability as the *stiffness*, since more stable lower layers are more resistant to penetrating motions.

Since the polytropic index is related to the hydrostatic heat flux and the total flux must be constant throughout the domain, S defines a relationship between the thermal conductivities, K_i, in the two layers, given by

$$\frac{K_2}{K_1} = \frac{m_2 + 1}{m_1 + 1} = \frac{S(m_{\rm ad} - m_1) + m_{\rm ad} + 1}{m_1 + 1}\,. \tag{3}$$

In practice in the simulations, this conductivity contrast between the convective and stable regions is imposed through a piecewise constant conductivity function (of $\tilde{z}$) with the discontinuous junction smoothed by a narrow ($\sim 0.1d$) hyperbolic tangent function. Note that θ represents the hydrostatic temperature gradient in layer 1, and therefore to maintain the total vertical heat flux through the system, the temperature gradient in layer 2 must be $(K_1/K_2)\theta$. This penetrative configuration imposes the thermal conductivity as a function of height instead of a more realistic function of temperature and density (e.g., Kramer's law). We have chosen this model for numerical considerations and because it allows direct comparison between these three-

dimensional simulations and previous two-dimensional numerical calculations. Comparable models using Kramer's law will be available soon (D. H. Porter & P. Woodward 2000, private communication).

The equations for the conservation of mass, momentum, and energy, and the equation of state for a perfect gas can be nondimensionalized using d as the unit of length, the isothermal sound crossing time at the top of the domain $[d^2/(c_p - c_v)T_0]^{1/2}$ as the unit of time, and T_0 and ρ_0 as the units of temperature and density, to produce

$$\partial_t \rho + \nabla \cdot (\rho \boldsymbol{u}) = 0 , \tag{4a}$$

$$\partial_t(\rho \boldsymbol{u}) + \nabla \cdot (\rho \boldsymbol{u}\boldsymbol{u}) = -\nabla p - P_r C_k T_{a_0}^{1/2}\left(\hat{\Omega} \times \rho \boldsymbol{u}\right) + P_r C_k \left[\nabla^2 \boldsymbol{U} + \frac{1}{3}\nabla(\nabla \cdot \boldsymbol{U})\right] + \rho g \hat{z} , \tag{4b}$$

$$\partial_t T + \nabla \cdot (\boldsymbol{u} T) + (\gamma - 2) T \nabla \cdot \boldsymbol{u} = \frac{\gamma C_k}{\rho} \nabla \cdot (K_z \nabla T) + V_\mu , \tag{4c}$$

$$p = \rho T . \tag{4d}$$

Here $\boldsymbol{u} = (u, v, w)$ is the velocity, T is the temperature, ρ is the density, and p is the pressure, and these are the state variables as functions of space (x, y, z) and time t. The rate of viscous heating is $V_\mu = [(\gamma - 1)C_k/\rho]P_r \partial_i u_j (\partial_i u_j + \partial_j u_i - \frac{2}{3}\nabla \cdot \boldsymbol{u}\delta_{ij})$.

A set of dimensionless numbers parameterize the problem. The Rayleigh number,

$$\mathrm{Ra}(z) = \frac{\theta^2 (m_i + 1)}{\mathrm{Pr}\, C_{k_z}^2}\left[1 - \frac{(m_i + 1)(\gamma - 1)}{\gamma}\right](1 + \theta z)^{2m_i - 1} , \tag{5}$$

measures the competition between buoyancy driving and diffusive effects, and thus the supercriticality and vigor of the convection. Ra involves the thermal dissipation parameter $C_{k_z} = C_k K_z$, where $K_z = K_i/K_1$ and $C_k = K_1/\{d\rho_0 c_p[(c_p - c_v)T_0]^{1/2}\}$. The latter is a thermal diffusion parameter representing the ratio of the sound crossing time to the thermal relaxation time in a layer. The total energy flux into the system is then $[\gamma/(\gamma - 1)C_k\theta]$. Here Ra is quoted as evaluated at the middle of the unstable layer in the initial polytrope.

The Prandtl number,

$$\mathrm{Pr} = \frac{\mu c_p}{K_1} , \tag{6}$$

defines the ratio of the diffusivities of momentum and heat, evaluated in the upper layer. Note that a complete Prandtl number $\mathrm{Pr}_z = \mu c_p / K_z$ takes different values in the different layers, but the diffusivity of momentum, $C_{k_z}\mathrm{Pr}_z = C_k \mathrm{Pr}$, is independent of K_z and therefore also of depth.

Rotation enters the momentum equation in a modified f-plane formulation in this local model via the rotation vector,

$$\Omega = \Omega_0 \hat{\Omega} = \left(\Omega_x, \Omega_y, \Omega_z\right) = (0, \Omega_o \cos\phi, -\Omega_o \sin\phi) , \tag{7}$$

where ϕ is the latitudinal positioning of the planar domain on the sphere. Notice that in the z-downward coordinate system, positive rotation is clockwise when viewed from above the north pole, the opposite of the intuitive planetary or solar rotation. The sense can be made more familiarly anticlockwise by setting $\Omega_0 \rightarrow -\Omega_0$ (equivalently $u \rightarrow -u, x \rightarrow -x$) when examining the results. The Taylor number,

$$\mathrm{Ta}_0 = \frac{4\Omega_0^2 d^4}{(\mu/\rho_0)^2} = \left(\frac{\rho}{\rho_0}\right)^2 \mathrm{Ta} , \tag{8}$$

measures the influence of rotation (as compared to diffusive effects). Here Ta (the more usual Taylor number) is quoted as evaluated at the middle of the unstable layer in the initial polytrope, for consistency with Ra.

A measure of the influence of the rotation on global motions derived in terms of these parameters is the convective Rossby number

$$\mathrm{Ro} = \left(\frac{\mathrm{Ra}}{\mathrm{TaPr}}\right)^{1/2} . \tag{9}$$

A value of Ro less than unity implies a significant influence of the rotation, since then in the time a fluid element is driven across the layer by buoyancy it can execute more than one inertial rotation. A true Rossby number Ro_t may be determined as the ratio of the root mean square (rms) vorticity generated in the convection to that of the rotating frame, i.e.,

$$\mathrm{Ro}_t = \frac{\omega_{\mathrm{rms}}}{2\Omega} . \tag{10}$$

It is found here that Ro and Ro_t are generally comparable.

In addition to the external control parameters, some measure of the degree of turbulence encountered in the resulting solutions is often required. The standard dimensionless parameter for this is a Reynolds number, indicating the relative balance between advective and diffusive processes. This may be defined by

$$\mathrm{Re}(z) = \frac{U(z)\overline{\rho}(z) l}{C_k \mathrm{Pr}} , \tag{11}$$

where l and $U(z)$ are a typical length and velocity, respectively. There are a number of possibilities for the choices of these characteristic values. We calculate and quote two types of Reynolds numbers here, both using the (time-averaged) rms velocity, U_{rms} as the characteristic velocity, but with one (Re) using the depth of the domain as the length scale, while the second (Re_λ) uses the Taylor microscale, λ. The latter scale is defined by

$$\lambda^{-2}(z) = \frac{\overline{V_\mu}(z)}{U_{\mathrm{rms}}(z)} \tag{12}$$

and represents the scale of dissipation associated with the rms velocity. In general here, a value of Re_λ greater than about 10, or Re of about 10^3 or greater, indicates a solution that is at least moderately turbulent.

A related quantity, the Péclet number, Pe, is defined by

$$\mathrm{Pe} = \frac{U(z)\overline{\rho}(z) l}{C_k} , \tag{13}$$

and is important for penetrative convection since it measures the relative importance of advective effects and thermal diffusion, the two ingredients determining the deceleration of a particle entering a stable layer. Characteristic scales may be chosen as above for the Reynolds number, but it will

also prove instructive to create a Péclet number solely for the downflowing plumes encountered in the simulations, using a typical length scale and velocity from only those regions (see § 3.7).

2.2. *Boundary Conditions*

At the upper and lower boundaries, we require that

$$\rho w = \partial_z u = \partial_z v = 0 \text{ at } z = 0, z_m\,, \tag{14a}$$

$$T = 1 \quad \text{at } z = 0, \qquad \partial_z T = \frac{K_1}{K_2}\theta \quad \text{at } z = z_m\,, \tag{14b}$$

which ensure that the mass flux and mechanical energy flux vanish on the boundaries. The total mass in the computational domain is conserved and the imposed heat flux is the only flux of energy into and out of the system. The heat flux is imposed at z_m such that, in the hydrostatic polytropic state, the temperature gradient at the interface $z = 1$ would be fixed at θ as required.

2.3. *Numerical Solution*

Equations (4) are solved numerically as an initial value problem by a semi-implicit, hybrid finite-difference/pseudospectral scheme. The vertical structure is treated by fourth-order finite differences in the interior. Forward and backward differences at the boundaries provide reflection criteria to ensure that the mass flux and mechanical energy flux vanish there and that the temperature conditions are satisfied. The horizontal components are treated by a Fourier collocation method that immediately ensures that the requirements of periodicity are fulfilled. The pseudospectral method calculates all linear operations and derivatives in spectral space (k_x, k_y, z) and performs the nonlinear multiplications in configuration space (x, y, z), with the transform between spaces achieved by fast transform methods. The time discretization is based on a three-level Adams-Bashforth scheme, which has good stability criteria and yet requires only one new evaluation and two storages on the nonlinear fluxes at every time step. The thermal conduction terms in the temperature equation are treated implicitly with a Crank-Nicolson method to avoid overly restrictive time-step constraints near the upper boundary where the density is low due to the stratification. We solve the full Navier-Stokes equations for fluid motions without recourse to adaptations to lessen the effects of viscosity. While this means that the Reynolds number, Re, is restricted by the resolution, it also means that no assumptions are imposed about the effective role of viscosity. The version of the code used for these studies has been extensively parallelized using message-passing and/or vendor memory-management routines and was run very efficiently on the massively parallel IBM SP-3, Cray T3E, and SGI Origin 2000 machines at resolutions up to $512^2 \times 575$.

3. PENETRATIVE CONVECTION

The problem as posed is governed by many dimensionless parameters engendering a large parameter space. In the solar context, these parameters are set by the nature of the star and in particular the properties of the gas. The solar values of many of these properties are not known exactly, but some order of magnitude estimates for the dimensionless numbers exist (see, e.g., Priest 1982). For example, it is estimated that the Reynolds number is of order 10^{12} or greater, and the Prandtl number is of order 10^{-8} or less. These parameters indicate that the solar gases are likely in very turbulent fluid motion. Such values are not currently attainable in numerical simulations. While we cannot simulate the Sun then, we hope to gain insight into some of the basic physical processes that might be occurring in the solar interior. Our aim here then is to investigate the dynamics of a turbulent fluid for a range of parameters that can be simulated with current resources and to ascertain which features could possibly be considered robust.

We therefore survey a portion of the parameter space as outlined in Table 1. Our primary calculations are based around an investigation of the effect of varying the relative stability, S, of the stable zone below the convective region. We use initial conditions based around a $\theta = 10, m_1 = 1$ polytrope with a $\gamma = 5/3$ gas in the convective region for all simulations, and then, unless otherwise specified, use the *benchmark parameters* $\mathrm{Ra} = 5 \times 10^5$ and $\mathrm{Pr} = 0.1$. These parameters correspond to a highly supercritical (more than 100 times critical) and therefore turbulent solution with a significant degree of background stratification (density contrast $\sim$25 across the convection zone). The convective part of the domain has aspect ratio $6 \times 6 \times 1$ $(x : y : z)$ for all simulations, but the full domain depth varies according to the stiffness of the stable region, ranging from $z_m = 2$ for the stiffest stable region considered ($S = 30$) to $z_m = 3.5$ for the most pliable ($S = 0.5$). These cases are directly comparable to the nonpenetrative cases of earlier studies (Cattaneo et al. 1991; Brummell et al. 1996, 1998). As well as considering the dependence on S, we also investigate the variation of selected cases with changes in degree of supercriticality (nonlinearity) and with rotation, including an examination of the effect of varying the latitudinal positioning of the f-plane domain. We begin here with a general description of the mechanism and characteristics of penetrating and overshooting convective motions, and define the measures necessary for quantifying the results.

3.1. *Overview of Penetrative Motions*

Figure 1 provides an overview of penetrative convection as compared to convection in a nonpenetrative purely convective domain. The figure shows two different views of typical snapshots from both nonpenetrative (case 0) and penetrative simulations (case 2) carried out at the benchmark parameters. Shown are volume renderings of the vertical velocity (Figs. 1*a*, 1*c*, 1*e*, and 1*g*) and the enstrophy density, $|\omega|^2$, where $\omega = \nabla \times \boldsymbol{u}$ is the vorticity (Figs. 1*b*, 1*d*, 1*f*, and 1*h*), with the upper four panels (Figs 1*a*, 1*b*, 1*c*, and 1*d*) drawn from a simulation with an impenetrable lower boundary at $z = 1$ (case 0) and the lower four (Figs 1*e*, 1*f*, 1*g*, and 1*h*) from a simulation of penetrative convection with $S = 1$ and a stable region spanning $1 \leq z \leq 2.5$ (case 2).

It has been understood for some time now from simulations of convection in local domains (e.g., Hurlburt et al. 1984; Stein & Nordlund 1989; Cattaneo et al. 1991; Porter & Woodward 1994; Brummell et al. 1996; Julien et al. 1996b) that the topology of turbulent convection differs from the cellular nature of laminar convection. As the Reynolds number increases, the simple cellular overturnings of laminar convection are replaced by a plume-dominated convective system. The thin turbulent boundary layers shed compact upflows and downflows, or plumes, which interact

TABLE 1

PARAMETERS AND MEASURED PENETRATION DEPTHS FOR THE COMPRESSIBLE PENETRATIVE CONVECTION SIMULATIONS

Case No.	Case Tag	Resolution n_x, n_y, n_z	S	z_m	C_k	Ra	Pr	Ta	ϕ	Ro	Δ_p
0	$S=\infty$	$128^2 \times 128$	∞	1.0	0.07	4.9×10^5	0.1	...	...	...	...
1	$S=0.5$	$128^2 \times 350$	0.5	3.5	0.07	4.9×10^5	0.1	...	...	...	0.94
2	$S=1$	$128^2 \times 350$	1	3.5	0.07	4.9×10^5	0.1	...	...	...	0.85
3	$S=2$	$128^2 \times 300$	2	3.0	0.07	4.9×10^5	0.1	...	...	...	0.73
4	$S=3$b	$128^2 \times 300$	3	2.5	0.07	4.9×10^5	0.1	...	...	...	0.57
5	$S=7$b	$128^2 \times 192$	7	2.0	0.07	4.9×10^5	0.1	...	...	...	0.40
6	$S=15$_3D	$128^2 \times 192$	15	2.0	0.07	4.9×10^5	0.1	...	...	...	0.32
7	$S=30$b	$128^2 \times 192$	30	2.0	0.07	4.9×10^5	0.1	...	...	...	0.28
(5)	$S=7$b	$128^2 \times 192$	7	2.0	0.07	4.9×10^5	0.1	...	...	∞	0.40
8	$S=7$b_rot1	$128^2 \times 192$	7	2.0	0.07	5.0×10^5	0.1	5×10^4	90	10.0	0.37
9	$S=7$b_rot2	$128^2 \times 192$	7	2.0	0.07	5.0×10^5	0.1	5×10^6	90	1.0	0.26
10	$S=7$b_rot4	$128^2 \times 192$	7	2.0	0.07	5.0×10^5	0.1	1×10^7	90	0.71	0.25
11	$S=7$b_rot2_p0	$128^2 \times 192$	7	2.0	0.07	5.0×10^5	0.1	5×10^6	0	1.0	0.25
12	$S=7$b_rot2_p15	$128^2 \times 192$	7	2.0	0.07	5.0×10^5	0.1	5×10^6	15	1.0	0.21
13	$S=7$b_rot2_p30	$128^2 \times 192$	7	2.0	0.07	5.0×10^5	0.1	5×10^6	30	1.0	0.15
14	$S=7$b_rot2_p45	$128^2 \times 192$	7	2.0	0.07	5.0×10^5	0.1	5×10^6	45	1.0	0.20
15	$S=7$b_rot2_p67	$128^2 \times 192$	7	2.0	0.07	5.0×10^5	0.1	5×10^6	67	1.0	0.22
(9)	$S=7$b_rot2	$128^2 \times 192$	7	2.0	0.07	5.0×10^5	0.1	5×10^6	90	1.0	0.26
16	$S=3$b_lo	$128^2 \times 300$	3	2.5	0.15	1.0×10^5	0.1	...	...	...	0.62
(4)	$S=3$b	$128^2 \times 300$	3	2.5	0.07	4.9×10^5	0.1	...	...	...	0.57
17	$S=3$b_hi	$128^2 \times 300$	3	2.5	0.05	1.0×10^6	0.1	...	...	...	0.54
18	$S=3$b_vhi	$256^2 \times 300$	3	2.5	0.02	5.0×10^6	0.1	...	...	...	0.46
19	$S=3$b_vvhi_a	$256^2 \times 300$	3	2.5	0.015	1.0×10^7	0.1	...	...	...	0.44
20	$S=3$b_vvhi_b	$256^2 \times 300$	3	2.5	0.011	2.0×10^7	0.1	...	...	...	0.35
21	$S=3$b_vvvhi	$512^2 \times 575$	3	2.5	0.0077	4.0×10^7	0.1	...	...	...	
22	$S=2$_low	$128^2 \times 300$	2	3.0	0.22	5.0×10^4	0.1	...	...	...	0.82
(3)	$S=2$	$128^2 \times 300$	2	3.0	0.07	4.9×10^5	0.1	...	...	...	0.73
23	$S=1$_low	$128^2 \times 350$	1	3.5	0.22	5.0×10^4	0.1	...	...	...	0.97
(2)	$S=1$	$128^2 \times 350$	1	3.5	0.07	4.9×10^5	0.1	...	...	...	0.85
24	$S=1$_vhi	$256^2 \times 350$	1	3.5	0.050	1.0×10^6	0.1	...	...	...	0.77
(17)	$S=3$b_hi	$128^2 \times 300$	3	2.5	0.05	1.0×10^6	0.1	...	...	...	0.54
25	$S=3$b_pr_lo	$128^2 \times 300$	3	2.5	0.07	1.0×10^6	0.05	...	...	...	0.55
(4)	$S=3$b	$128^2 \times 300$	3	2.5	0.07	4.9×10^5	0.1	...	...	...	0.57
(25)	$S=3$b_pr_lo	$128^2 \times 300$	3	2.5	0.07	1.0×10^6	0.05	...	...	...	0.55
26	$S=3$b_pr_vlo	$256^2 \times 300$	3	2.5	0.07	2.0×10^6	0.025	...	...	...	0.54

NOTE.—All simulations also have $\theta = 10, \gamma = 5/3, m_1 = 1, x_m = y_m = 6$. Case numbers in parentheses are cases repeated in the table for ease of comparison of solutions. The penetration factor Δ_p is measured in units of the convection zone depth. To convert to units of the pressure scale height, multiply the values by 2 (approximately).

or breakup in the interior to form small-scale turbulent motions (Fig. 1*b*). The asymmetry imposed by stratified compressible convection (Hurlburt et al. 1984) emphasizes this difference. A seemingly laminar surface network of downflows, with downward-directed plumes concentrated at the interstices of the network (Fig. 1*a*), masks the small-scale turbulent interior (Cattaneo et al. 1991). The latter is created from secondary instabilities and interactions of the plumes, as they concentrate and accelerate in the strengthening density background, eventually "splashing" against the lower boundary. The plume structures themselves can be turbulent and can be very complicated at very high Re (D. H. Porter et al. 1990; Porter & Woodward 1994).

The replacement of the lower impenetrable boundary with a bounding stable layer leads to substantial differences (Figs. 1*e*, 1*f*, 1*g*, and 1*h*). Most obviously, a downflowing plume that would previously have been forcibly turned as it impinges upon the lower wall is now afforded a more gentle deceleration by the pliable fluid below. Motions can extend beyond the convective layer, overshooting into the originally stable lower region. This has been anticipated in the astrophysical context for some time (e.g., Schmitt et al. 1984; Zahn 1991) and observed previously in numerical simulations in both two dimensions (Hurlburt et al. 1986, 1994; Jennings et al. 1992) and three dimensions (Nordlund et al. 1992; Singh et al. 1994, 1995; Saikia et al. 2000). It can be seen clearly in Figures 1*e* and 1*g* that vertical motions readily extend past the $z = 1$ line demarking the interface between the convectively driven layer with the stable zone. Some weaker and more diffuse up and down motions can also be detected (Fig. 1*g*) deep in the stable layer. These may be associated with internal gravity waves excited by the downflows impinging on the stable layer.

The companion pictures, Figures 1*f* and 1*h*, show the corresponding enstrophy densities. These fields generally offers a clearer depiction of the flow in terms of the plumes and other vorticity elements associated with the turbulence. Strong vertical tubelike vortices can be seen to be associated with the junctions of the upper surface network in w. These are coherent structures (in time and space) that represent the major downflow sites of the compressible convection (see also Cattaneo et al. 1991; Brummell et al. 1996, 1998). Smaller scale vorticity can be seen to be related to the deceleration of these downflowing plumes in the stable region, just below the interface. The structure of this enstrophy density field should be contrasted with that associated with the

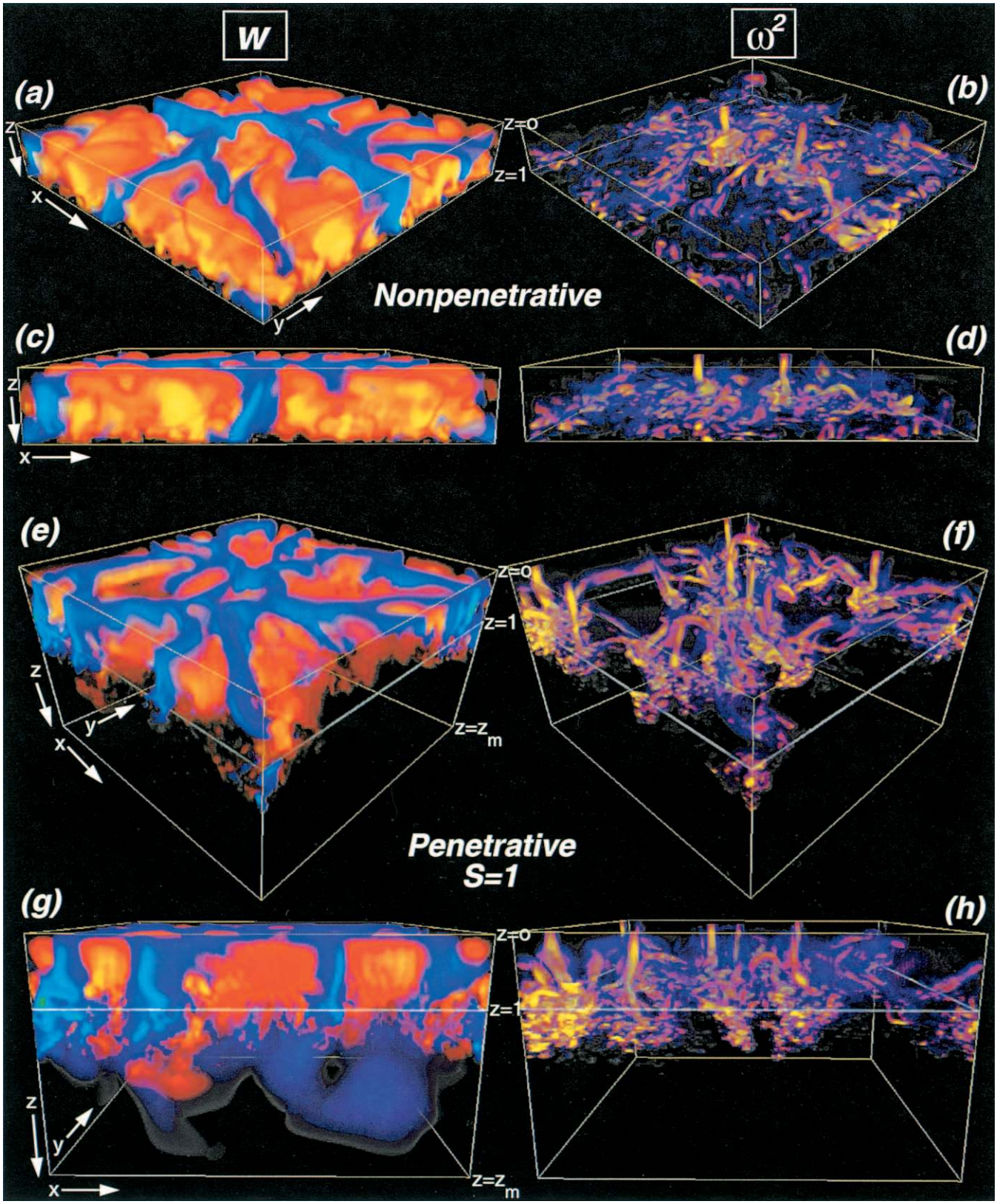

FIG. 1.—Comparison of penetrative and nonpenetrative simulations. Shown are volume renderings from a representative time of (*a*, *c*, *e*, and *g*) the vertical velocity w and (*b*, *d*, *f*, and *h*) the enstrophy density ω^2, where $\omega = \nabla \times \boldsymbol{u}$. Here and in subsequent volume renderings, the vertical velocity is colored so that yellow-red depicts upflowing material and light blue-blue is downflowing. The enstrophy density has strong values exhibited as white-yellow, intermediate values as purple, and weaker values as blue-black. In both cases, the opacity of the field is tied to its absolute value, so that strong values appear opaque whereas weak values appear translucent. This figure shows two different view points, from above and to the side, for two simulations at the benchmark parameters ($\mathrm{Ra} = 5 \times 10^5, \mathrm{Pr} = 0.1, \mathrm{Ta} = 0, \gamma = 5/3, \theta = 10, m_1 = 1,$ and $x : y : z = 6 : 6 : z_m$), but where one (*a–d*) has an impenetrable, stress-free lower boundary at $z = 1$, whereas the other (*e–h*) is a penetrative solution (case 2) with $S = 1, z_m = 3.5$.

nonpenetrative convection. Most noticeable is the quieter interior of the convection zone in the penetrative case, with less small-scale turbulent motion there. This is due to a less direct connection between the upflows and downflows. The small-scale turbulence is most likely a result of secondary shear instabilities (Cattaneo et al. 1991) and breakup of the fast downflows where they decelerate rapidly. With the pliable penetrative interface, the deceleration is not as rapid, and the return upward flow is not generated immediately by the enforced turning at an impenetrable wall. The net result is that less small-scale turbulent vortex action is generated and it is less likely to be carried straight into the interior of the convective domain. This has a number of consequences for mixing and transport, as will be discussed later.

3.2. *Mechanism of Penetration and Overshooting*

A more quantitative understanding of the mechanism for these extended motions can be gleaned from an examination of the thermodynamics of the flow via mean variables and fluxes. The mean temperature $\overline{T}$ and density $\overline{\rho}$ (where $\overline{X}$ represents the average of X over the two horizontal directions) define the mean thermodynamic state. The total heat flux available and its division into the adiabatic part and the superadiabatic part that drives the convection are

$$F_{\rm tot} = \frac{\gamma}{(\gamma-1)} C_k \theta \,, \tag{15a}$$

$$F_{\rm ad} = C_k \theta (m+1) \,, \tag{15b}$$

$$F_{\rm sub} = F_{\rm tot} - F_{\rm ad} \,. \tag{15c}$$

Energy fluxes may be defined from the kinetic energy and total energy equations as follows:

$$F_k = \frac{1}{2} \rho w |\boldsymbol{u}|^2 \,, \tag{16a}$$

$$F_e = \frac{\gamma}{\gamma-1} \rho w T' \,, \tag{16b}$$

$$F_p = w p' \,, \tag{16c}$$

$$F_r = C_k K_z \frac{\gamma}{\gamma-1} \partial T / \partial z \,, \tag{16d}$$

$$W_b = \theta (m+1) w \rho' \,. \tag{16e}$$

These are the kinetic, enthalpy, acoustic and radiative fluxes, and the buoyancy work, respectively, involving the fluctuating variables $T' = T - \overline{T}$, $p' = p - \overline{p}$, and $\rho' = \rho - \overline{\rho}$. We will also refer to

$$F_{\rm ra} = F_r - C_k \theta \gamma / (\gamma - 1) \,, \tag{17a}$$

$$F_c = F_e + F_k \,, \tag{17b}$$

$$F_T = F_c + F_{ra} \,, \tag{17c}$$

which are the radiative flux adjusted by the $F_{\rm tot}$, the convective flux, and the total flux in the convective state (where the latter two omit the negligible viscous flux).

The three quantities F_e, F_p, and W_b are correlations between the vertical velocity and the thermodynamic fluctuations, and the horizontal averages of these fluxes, denoted by an overbar [e.g., $\overline{F_k(z,t)}$], give the net vertical transport of the quantities across a horizontal plane at any time. A detailed study of the energetics of nonlinear convection that includes a discussion of the roles of the quantities above can be found in Hurlburt et al. 1984. Since all of the simulations described here achieve a statistically steady state, the horizontal mean fluxes are further averaged over time to produce a function purely of the vertical variable denoted by angle brackets, e.g., $\langle F_k(z) \rangle$.

The model for the penetrative system used here is defined in terms of a polytropic hydrostatic state with a thermal background created such that the upper layer is convectively unstable and the lower layer is stable. In terms of the polytropic indices, this requires that the upper layer have index $m_1 < m_a$ and the lower layer $m_2 > m_a$, where $m_a = 1/(\gamma - 1)$. This defines a mean temperature and density profile, such that the entropy gradient is positive in the upper layer and negative in the lower layer, ensuring the required stability criteria in the layers. An example of these is shown in Figure 2, together with the statistically steady state profiles that the simulation relaxes to, for the simulation at the benchmark parameters with $S = 7$ (case 5). The dashed line profiles are the polytropic states, and the solid lines the simulation results. In the absence of motions, the fixed imposed flux of heat is carried by radiation, and then the temperature gradient in the two layers is fixed by the ratio of the conductivities (eq. [3]), with the upper gradient fixed at the input value of θ (Fig. 2*b*). When motions set in as a result of the convective instability in the upper layer, the temperature gradient in the relaxed state must return to the original values at the boundaries, but a number of thermodynamic effects due to the induced convective mixing will affect the interior. First, the overall stratification sags, redistributing density such that the mean increases in the lower layer and decreases in the upper layer (Fig. 2*c*). This is a standard feature of compressible simulations formulated in this way and simply implies that polytropes are artificially top heavy. The mean temperature cools overall (Fig. 2*a*), as it is allowed to do since only the flux is imposed as a lower boundary condition. Convection then acts in its natural manner to remove the driving gradient in the bulk of the overturning flow. The entropy gradient (Fig. 2*d*) shows that the interior becomes close to isentropic (adiabatic) in the interior of the convection zone. The temperature gradient is also reduced there (Fig. 2*b*), and then this temperature gradient matches to the polytropic radiative values both at the upper boundary and where the motions die out below the interface in the lower stable region. In this latter matching region, the entropy gradient switches from positive (unstable) to negative (stable) as it must, but the switching point is not necessarily exactly at $z = 1$, owing to the redistribution of the background stratification by the convective mixing. In the example shown, the adiabatic region does not appear to extend below $z = 1$, indicating that, technically, overshooting is taking place but not penetration. The feedback on the mean stratification may be somewhat limited by the fact that the thermal diffusivity is dependent only on depth and not on the temperature or density, and this may effect the structure of the adiabatic region and its transition to subadiabaticity. However, preliminary analyses of simulations where this restriction is not present since a Kramer's law conductivity function was used (D. H. Porter & P. Woodward 2000, private communication), appear to show similar results for the mean thermodynamic balances. The feedback process, and therefore the termination of the adiabatically mixed region, certainly depends on the parameters of the problem, in particular the relative stiffness of the stable layer and the Péclet number. However, the lack of an

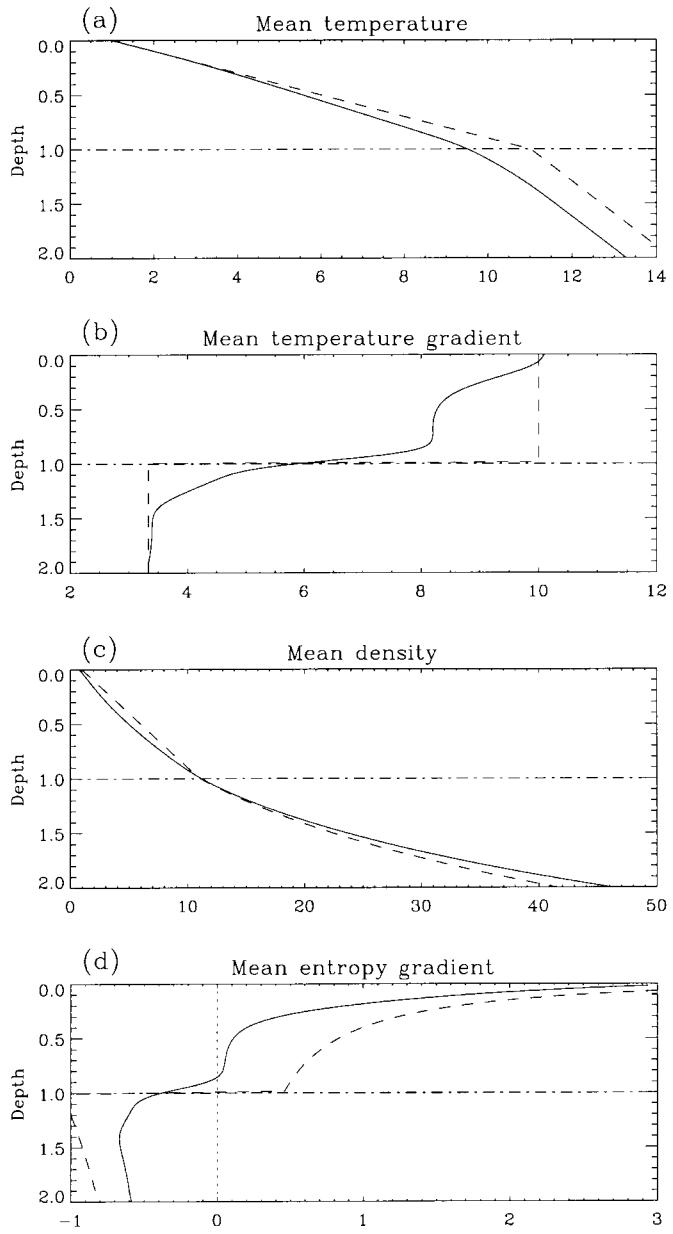

FIG. 2.—Mean stratification in an example penetrative simulation (case 5). The dashed lines represent the stratification for the piecewise polytrope initial condition upon which the penetrative model is based. The solid line shows the nonpolytropic background state of the statistically steady state attained in the time integration of the model. The profiles shown are horizontal and time averages of (*a*) the mean temperature, (*b*) its gradient, (*c*) the mean density, and (*d*) the mean entropy gradient.

extended adiabatic region appears to be a robust feature of all our three-dimensional simulations as will be discussed in detail later.

Having exhibited the underlying mean state, the time- and horizontally averaged fluxes shown in Figure 3 illustrate how the fluctuations about these means act in the convective motions. This plot shows the contributions to $\langle F_e \rangle, \langle F_k \rangle, \langle W_b \rangle$, and the total convective flux, $\langle F_c \rangle = \langle F_e + F_k \rangle$, from different portions of the flow—the upflows, the downflows, and the strong downflows—as functions of depth. Here a downflow is declared strong if its value is greater than 40% of the maximum value of $|w|$. While this thresholding method is not an ideal representation of the coherent structures, it does provides some indication of the contribution from plumelike downflow structures.

The kinetic flux $\langle F_k \rangle$ clearly illustrates the extended motions. The asymmetry of compressible convection, where downdrafts are narrow and updrafts are broad, leads to a downward-directed (positive) kinetic flux (Hurlburt et al. 1984). The nonzero value of this kinetic flux for some depths below $z = 1$ indicates the existence of substantial motions in the stable region. Since the contributions to the kinetic flux are dominated by a term proportional to w^3, the positive flux stems mainly from the downflows, with a major contribution from strong downflows, cancelled in part by the small negative effect of the upflows. It is clear from such analysis and from the overviews of the flow (Fig. 1) that plumes plunge into the stable layer and stir up motions there. The peak kinetic flux occurs just above the interface and the motions die out by about $z = 1.5$ in this case. Measures of the extent of these motions and their dependence on the parameters of the model are the main topic of this paper and will be addressed shortly.

The motions eventually die out in the stable region where the convective driving is absent, i.e., where the entropy gradient becomes subadiabatic (negative). In the original formulation, the division between stable and unstable, as defined by imposed regions of sub- and superadiabaticicity, was exactly at $z = 1$. However, feedback from the convective overturnings adjusts the positioning of these regions somewhat. After traversing the slightly superadiabatic convection zone, the negative entropy perturbations of the downward motions switch sign relative to the mean, and the motion is decelerated. This is most clearly demonstrated by the buoyancy work, $\langle W_b \rangle$, of the downflows (Fig. 3*c*). This measure is related to the density perturbations, which are somewhat easier to interpret than the entropy perturbations. A positive value of W_b corresponds to less dense fluid moving upward or more dense fluid moving downward, as is typical in convection. A negative W_b indicates the opposite, with less dense fluid moving downward or more dense fluid moving upward. This less intuitive situation represents buoyancy braking or deceleration of the motions. Figure 3*c* clearly shows this braking in the downflows in the subadiabatic region, down to the level where motions cease. There is a small region of negative buoyancy work in the upflows at the start of the subadiabatic region that probably corresponds to *splashing*; some downflowing dense fluid impinging upon the stiffer layer is turned rapidly upward by pressure gradients forming small pockets of upward-moving dense fluid. Lower down, the upflow profile of W_b returns to a positive value where downflows become warmed, expand, and begin to rise, creating the return upflows for the convective motions. The overturning motions of convection appear to be much more disconnected in the penetrative case when compared to the nonpenetrative. The main return flows in overshooting convection originate deep in the stable layer and are associated with the penetrating plumes, which are not very space filling. There is somewhat of a splash layer, but this is much less active than the return flows associated with an impenetrable wall. Notice also that there is a small amount of buoyancy braking in the upflows near the upper boundary too owing to the competition of pressure and temperature effects, as was noted and explained in the two-dimensional simulations of Hurlburt et al. (1984).

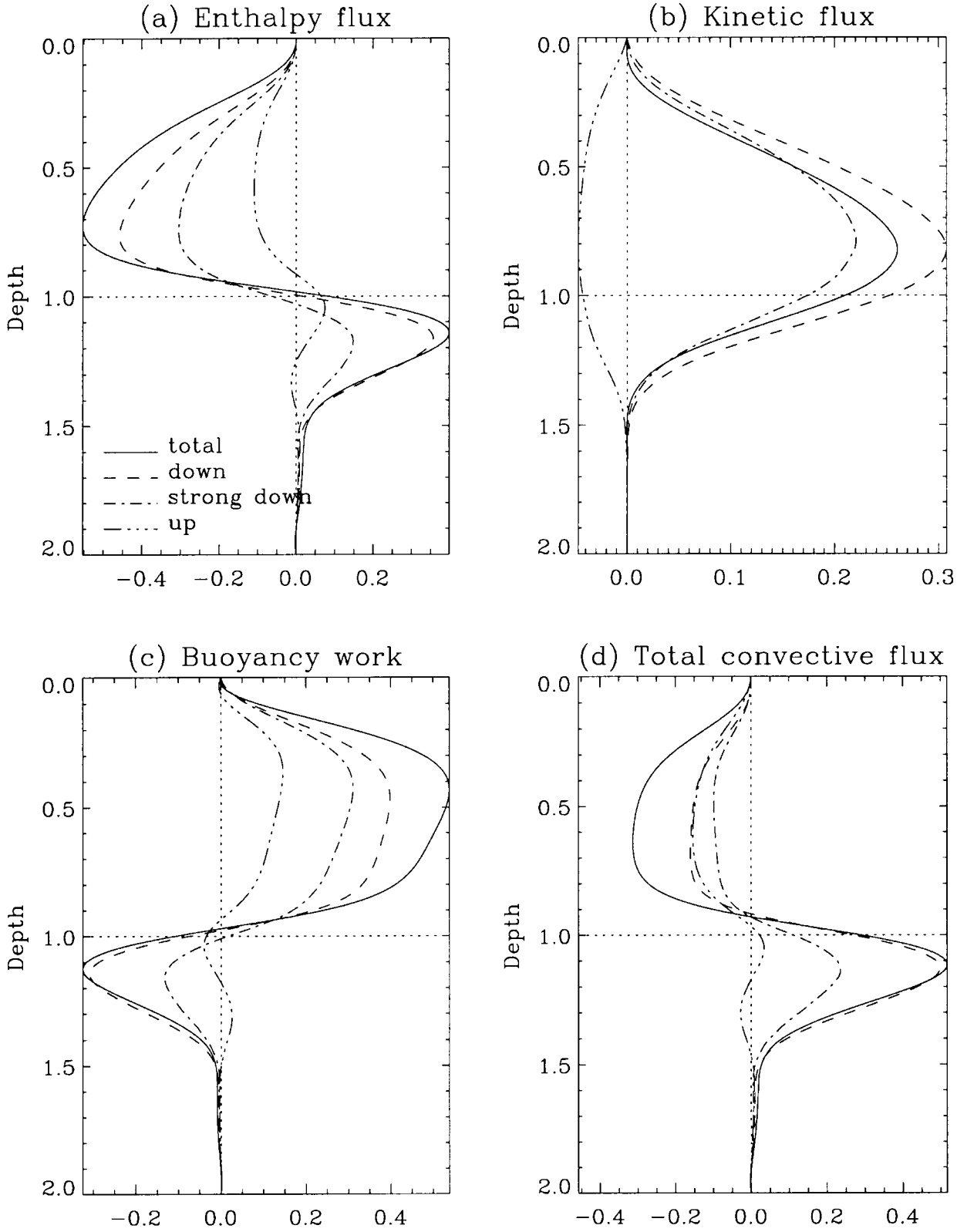

FIG. 3.—Example of the mean fluxes in a penetrative calculations and their distribution among different components of the flow. Shown from case 5 are the time- and horizontally averaged (*a*) enthalpy flux $\langle F_e \rangle$, (*b*) kinetic flux $\langle F_k \rangle$, (*c*) buoyancy work $\langle W_b \rangle$, and (*d*) total convective flux $\langle F_c \rangle = \langle F_k + F_e \rangle$. For each, the solid line exhibits the total mean flux, whereas the dashed line represents the contribution from the downflows and the triple-dot–dashed line shows the component from the upflows. The single-dot–dashed line shows the contribution from the strong downflows, where strong is arbitrarily defined as any value greater than 40% of the maximum value of $|w|$.

Figure 3*a* shows the corresponding enthalpy transport, indicating clearly that heat is transported upward in the convectively driven region as expected, whereas in the stable zone, heat appears to be carried in the wrong direction. This effect reflects the temperature equivalent of the density result exhibited in the buoyancy work. The effect is mainly due to the downflows, where the change in sign of the entropy perturbations at the unstable-stable zone interface is achieved by changing signs in the temperature and density perturbations relative to their respective means. The downflows in the stable zone are suddenly warm relative to their surroundings, owing to a change in the background stratification, and so heat is carried downward until diffusion smooths out the perturbation or buoyancy braking forces the motions to cease.

3.3. *Measures of the Extent of Penetration and Overshooting*

The most immediate questions related to penetrative convection are associated with how far the motions penetrate and/or overshoot, and how these results depend on the parameters of the problem. To answer such questions, we require definitions of an instantaneous and then a time-averaged penetration depth that describe where motions overshooting into the stable layer cease. Such measures have traditionally been defined using the kinetic flux (see, e.g., Hurlburt et al. 1986, 1994; Singh et al. 1994; Saikia et al. 2000) since it is directly related to the motions and is conveniently signed. Previous calculations have marked the cessation of convective motions as the first zero of this signed quantity found in the stable layer below the interface. Here we still use the kinetic flux as the variable of interest, but use instead the point at which $\overline{F_k}$ reaches a certain fraction, δ_k, of its maximum value. A factor of 1%, or $\delta_k = 0.01$, has been used for the results displayed here (this choice is justified in the next section). While all the measures are related to the depth where the kinetic energy of the flow has dropped significantly, the latter description is somewhat more consistent. First, the measure can be defined in this manner using the unsigned mean kinetic energy instead of the signed kinetic energy flux if required. We have found that similar results are reported both ways. Second, the measure we use is always defined, whereas the zero crossing is not always present in $\overline{F_k}$. This fact also makes our measure more consistent in the sense that the average of its instantaneous values of $\overline{F_k}$ is approximately equal to the measure evaluated on the time-averaged kinetic flux $\langle F_k \rangle$. This not necessarily true of the earlier definition since the time average may end up with no zero crossing. Clearly, in the limit $\delta_k \to 0$, the measure defined here approaches that of the earlier publications if there exists a zero crossing in $\overline{F_k}$.

Figure 4 shows how a measure of the penetrating motions of this type is constructed, using the simulation case 5 shown in the previous figures as an example. Figure 4*a* shows the horizontally averaged kinetic flux, $\overline{F_k}(z,t)$, as a function of depth and time. The form of these curves does not depart drastically from the average (shown earlier in Fig. 3*b* and here in Fig. 4*c*), yet exhibits some time-dependence reflecting activity in the turbulent convective flow. From these curves, we can extract the *time-dependent penetration depth*, $z_p(t)$, as that depth (away from the upper boundary) where the kinetic flux

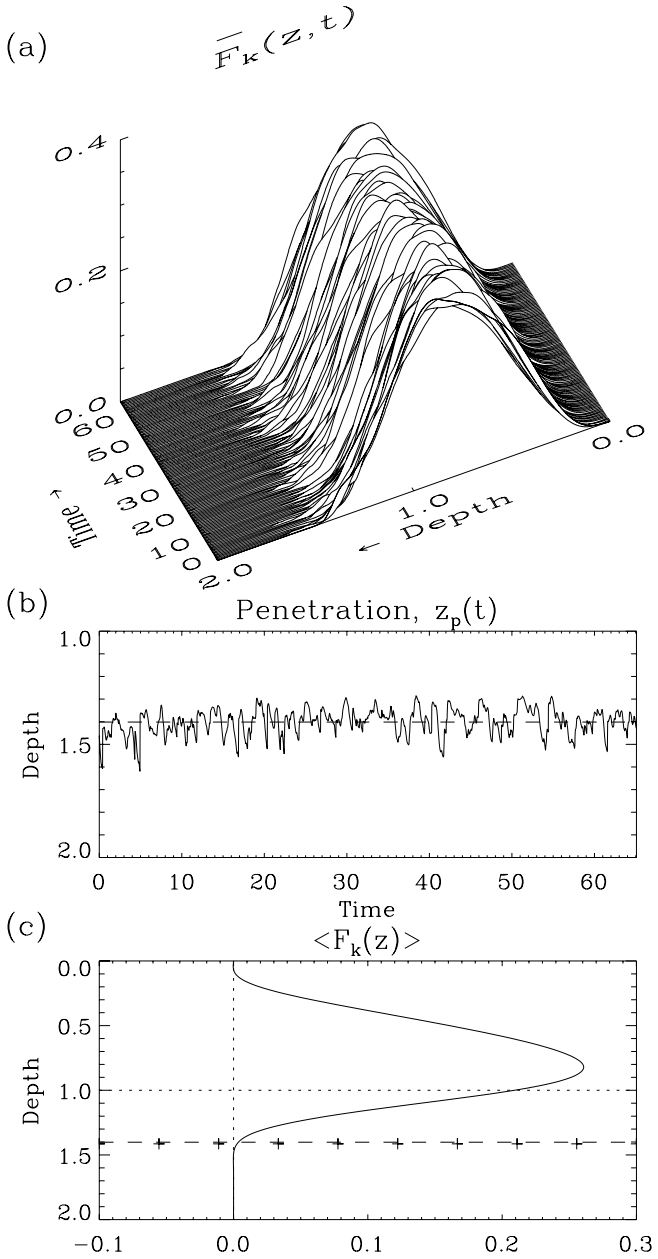

FIG. 4.—Illustration of the measurement of the penetrating and overshooting motions. Using case 5 as the example, (*a*) shows the horizontally averaged kinetic flux $\overline{F_k}$ as a function of time, *t*; (*b*) shows the time series of $z_p(t)$ extracted from the kinetic flux, with its time average z_o indicated as the horizontal dashed line; and (*c*) shows the time-averaged mean kinetic flux $\langle F_k \rangle$, with the calculated levels z_{om} and z_o indicated by the crosses and the dashed line, respectively.

falls to δ_k of its maximum value, i.e.,

$$z_p(t) = z\left|\left\{\overline{F_k(z,t)} = \delta_k \max\left[\overline{F_k(z,t)}\right]\right\}\right. . \qquad (18)$$

Figure 4*b* shows the time series of z_p for this example. The measure is time-dependent but with a well-established mean indicated on the plot by the horizontal dashed line. We will designate this mean value as the *overshoot depth*, z_o. This value is also shown on Figure 4*c*, which plots the time-averaged value of the mean kinetic flux, $\langle F_k \rangle$ as a function of depth. The crosses on this plot denote the penetration depth, z_{om}, obtained by using this mean curve only, and it

can be seen that the values correspond closely ($z_o = 1.43$ and $z_{om} = 1.41$). The penetration depth in numerical simulations has traditionally been quoted as the fractional increase in depth of motions below the original convection zone depth, and so we define the *penetration fraction*, $\Delta_p = z_o - 1$. For practical purposes, it may be more sensible to quote the depth in terms of the pressure scale height H_p at the bottom of the convective layer. We note here that $H_p(z = 1)$ under the polytropic initial conditions is $(1 + \theta)/[\theta(m_1 + 1)] = 0.55$, and is the same for all our simulations. The nonlinear states that the simulations relax to, however, are not polytropes and provide a somewhat different (and case dependent) value for H_p, ranging between $0.45 \leq H_p \leq 0.49$. In general here, we quote Δ_p, but a value in terms of the pressure scale height is always roughly twice as large.

3.4. *Dependence of δ_k: Gravity Waves*

These penetration measures of course depend on the choice of δ_k. We therefore present Figure 5, illustrating what the measure represents for different values of δ_k, to justify our choice of δ_k. Figure 5*a* shows a time trace of the penetration depth $z_p(t)$ for a small time interval extracted from an example simulation (case 3) for three different small values of $\delta_k = 0.01,\ 0.005,\ 0.0025$. In this plot, horizontal lines of the same line style as the time traces mark the values of z_o calculated for each δ_k (and they are marked as arrows in Figs. 5*b*, 5*c*). The three time traces agree fairly closely, and only during specific events do they disagree significantly. The question is whether these specific events should rightfully be included in the penetration measure or not. For example, an event is occurring at $t = 10.2$ (*solid vertical line*) that is being picked up by the smaller values of δ_k, but not by the largest value. A plot of the kinetic energy flux at $t = 10.2$ from which these measures were derived is shown as Figure 5*b*. The levels that the various δ_k pick out as the penetration depths $z_p(t = 10.2)$ are shown as horizontal dot-dashed lines. The end of the strong kinetic flux variation is chosen by the largest value of δ_k, but a small positive tail is picked up by the smaller values. Since $\overline{F_k}$ is an average measure, this weak tail could possibly correspond to a significant deep plume event that fills little space, a result that would be interesting. However, Figure 5*c* shows that this is not the case. This gray-scale plot shows a two-dimensional map of the maximum of the kinetic energy taken over the third dimension (the line of sight) at the time of the event under consideration ($t = 10.2$). The horizontal dot-dashed lines again correspond to the $z_p(t = 10.2)$ associated with the three δ_k. For clarity, the gray scale is scaled independently for the portions above and below the solid triangle pointer on the left. It can be seen that strong (*light colored area*) kinetic energy can be found down to the level of z_p formed from $\delta_k = 0.01$ (*top dot-dashed line*) but that between this line and the left triangle pointer the plot is solid black. If the map was *not* rescaled below the left triangle pointer, the whole map below the line for $z_p(\delta_k = 0.01)$ would be black. This indicates that the kinetic energy values are much weaker *everywhere* below the first dashed line than above, and thus there is no evidence for a small highly energetic region, such as a plume, below that level. We have rescaled the region below the left triangle pointer so that the topology of the *weak* kinetic energy fluctuations shows up. It can then be seen that large-scale gentle motions do exist lower down, and these are responsible for the weak tail in $\overline{F_k}$. These motions are associated with gravity waves generated in the stable layer by the impinging plumes and are not related to any significantly deep penetration event. It appears that a value of $\delta_k = 0.01$ generally gives good results concerning the plume-driven penetration, while excluding gravity wave motions.

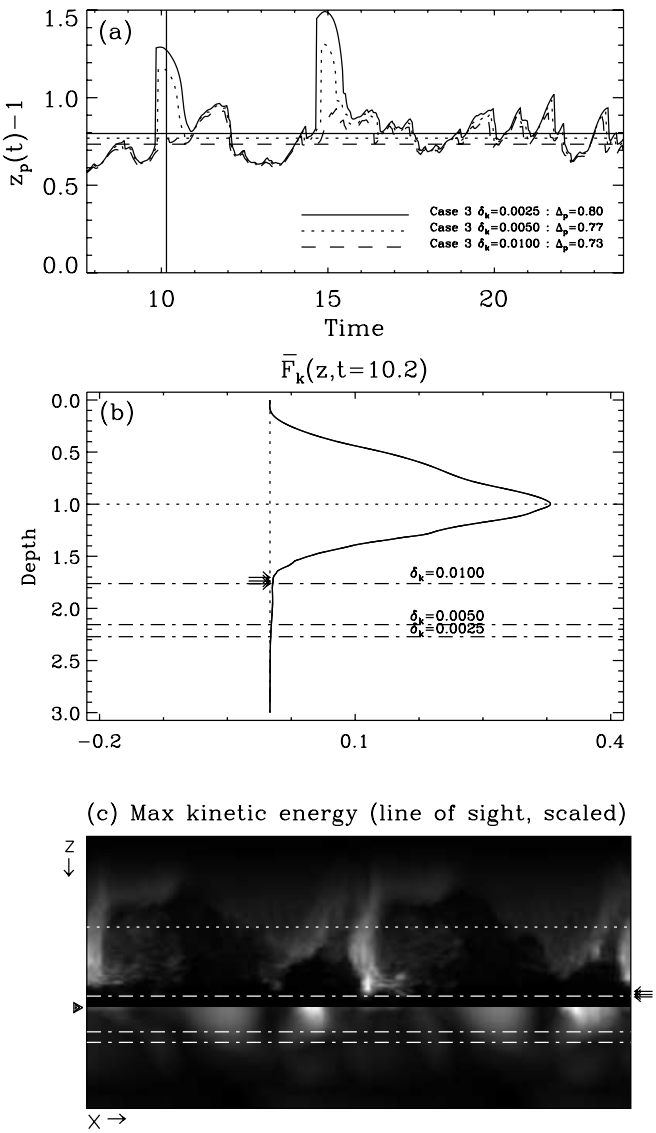

FIG. 5.—Filtering of the effects of gravity waves from the measurement of the penetration and overshooting using δ_k. Using case 3 as an example, (*a*) shows an excerpt from the time series for $z_p(t) - 1$, where a couple of seemingly deep events show up for small values of δ_k. The series for three different δ_k ($\delta_k = 0.0025$: *solid line*; $\delta_k = 0.005$: *dotted line*; $\delta_k = 0.01$: *dashed line*) are shown superimposed. The vertical line at $t = 10.2$ marks the event examined in the subsequent panels. The horizontal lines of the same styles (and the arrows in the subsequent panels) show the three similar averaged values of z_o corresponding to these different δ_k; (*b*) shows the mean kinetic flux $\overline{F_k}$ at $t = 10.2$ (*solid line*). The three widely varying instantaneous $z_p(t = 10.2)$ for the three values of δ_k are shown as the horizontal dot-dashed lines here (and in the next panel); (*c*) shows a two-dimensional (x-z) gray-scale plot of the maximum kinetic energy down the line of sight (the third dimension, y), thereby displaying any significant motions in the full domain. The gray-scaling is done independently above and below the black triangle pointer on the left in order to show up the gravity waves in the lower portions of the domain below the triangle.

It should be noted that these measures cannot fully represent the mechanism of penetration, by virtue of their averaged nature. A better measure of penetration would be defined on the extent of overshoot of individual plumes, but this is difficult since it is not simple to identify turbulent plumes in a robust and practical manner. Despite this, since most theories assume a mean effect of numerous plumes and many of the interesting questions address the level to which such penetrating flows affect the mean structure of the environment, our approach will suffice for now.

3.5. *Time Dependence: Impulsive Events*

Before addressing the dependence of the time-averaged penetration fraction Δ_p on the parameters, we would first like to comment on the time dependence of the overshooting motions. Figures 4*a* and 4*b* show there is a significant fluctuation of the penetrative measures about the mean value. While the aspect ratio of our domains are not enormous ($x : y : z = 6 : 6 : 1$), there are a significant number (at least $\sim$10, depending upon the parameters) of strong, coherent plumes present at any one time in the domain. A calculation with a much larger horizontal extent may give a less time-dependent value of $z_p(t)$; we have effectively replaced a larger domain average by a time average to obtain the relevant plume and penetration statistics. Either way, the question of the distribution of penetrating plumes is interesting. Figure 6 presents histograms of the distribution of $\Delta_{pt} = z_p(t) - 1$ (the time-dependent equivalent of Δ_p) for the time series of three of the simulations at different stiffnesses ($S = 1, 7, 30$ [cases 2, 5, and 7]). The figure shows the mean value, z_o, for each distribution as a vertical dotted line and also quotes the second and third moments of the distribution (m_2, the variance, and m_3, the skewness). While the variation of the mean with S will be discussed shortly, we note here that each distribution is asymmetric, with a distinct tail containing great numbers of plumes at higher values of Δ_{pt} than lower. This is quantitatively reflected in the positive skewness values. The distribution of Δ_{pt} is biased toward penetration events that are deeper than the mean. Furthermore, the increasing skewness with decreasing S seems to reflect a greater ease of deep penetration with a more pliable interface.

Once again, since the measure Δ_{pt} is a spatially averaged measure, this result does not give us any direct information about the possibility of deep penetration by individual plumes, although the distribution indicates that this is likely. We can check this conjecture by examining particular events in the $z_p(t)$ time series and analyzing their source. An example of this is shown in Figure 7. This figure is similar to Figure 5 except that it exhibits case 5, and Figure 7*c* shows a slice of the vertical velocity field instead of the kinetic energy measure of before. Figure 5*a* shows the penetration depth (over a short time interval extracted from the full simulation) where a number of deep events appear to be occurring. All three δ_k agree closely for the event chosen for examination at $t = 41.5$. Furthermore, unlike the previous example, Figure 5*b* shows that this event corresponds to a genuine deepening of the kinetic energy flux profile, rather than merely a weak additional tail induced by gravity waves. This

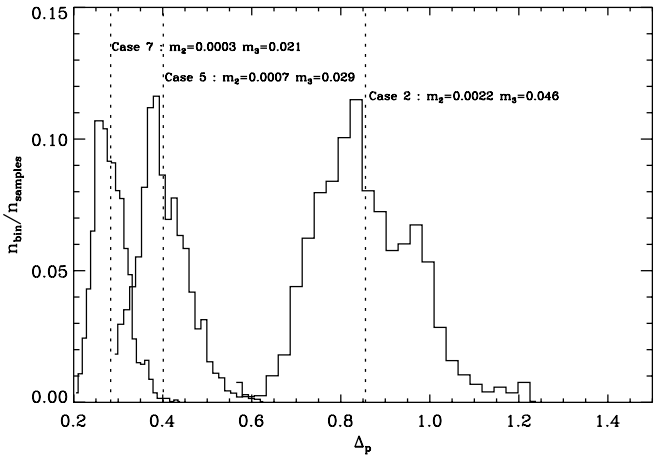

FIG. 6.—Histograms of the distribution of Δ_{pt} for three simulations, cases 2, 5, and 7. The means of the distributions are shown as vertical dotted lines, and the higher order moments (m_2, the variance, and m_3, the skewness) are annotated.

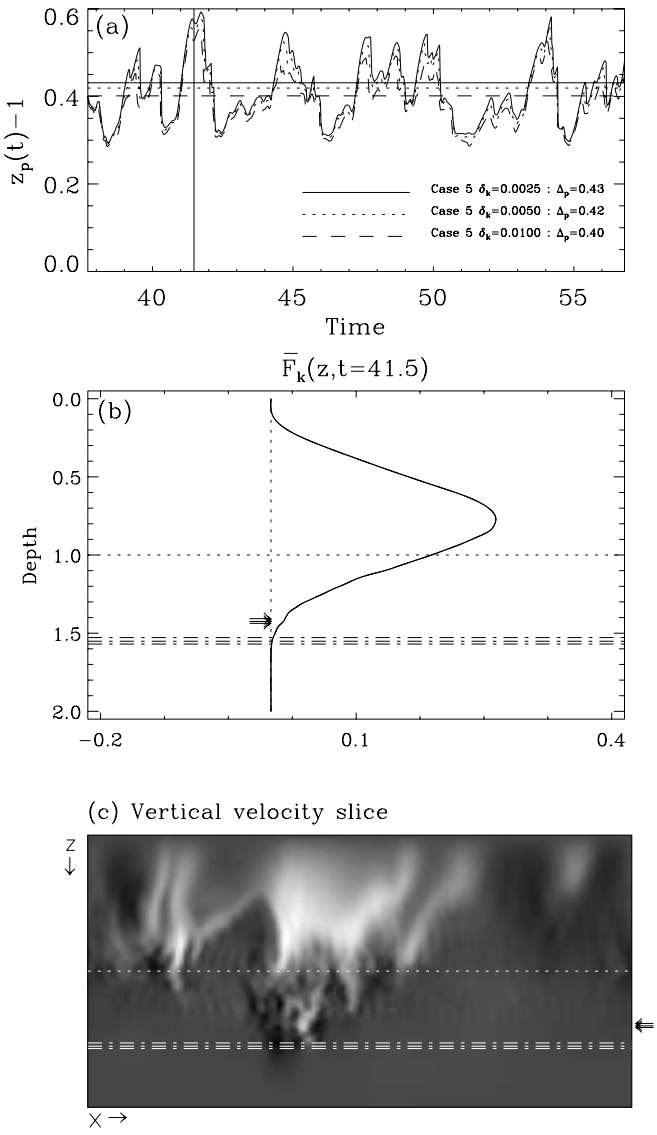

FIG. 7.—Illustration of a significant deep overshooting event from case 5. This figure is similar to Fig. 5 except that (*c*) shows a two-dimensional gray-scale plot of a particular slice of the vertical velocity field w where a strong plume can be seen.

latter evidence leads us to suspect that actual penetration events rather than gravity wave responses are causing the penetration depth changes. Indeed, on examining the velocity field associated with this time, for example the slice shown as Figure 5*c*, we can clearly see a strong downflow event providing enough influence to deepen $\overline{F_k}$ and z_p.

The events generating such deep penetration can be either exceptional individual plumes or can result from a strong interaction of a number of already strong plumes (as in the case in Fig. 7). This is not a rare occurrence, as shown by the time series $z_p(t)$ and the tails in the histograms, and examples such as this one can be found in all cases. In corroboration, a time series or animation of the kinetic flux profiles often shows the arrival of these strong events as a disturbance propagating downward through the profile. The timescale for these deeper penetrating events appears to be on the order of 20–25 time units. This number is comparable with estimates of a large-scale overturning time (based simply on the rms velocity and the average plume separation), although no large-scale overturning really exists. The coherence time for the velocity field is significantly shorter, on the order of 5–7 time units, and so these events, while fairly regularly spaced, are relatively infrequent. The extent of penetration, as measured by the horizontally averaged measure Δ_{pt}, which tends to smooth the actual events somewhat, can be increased by up to 50% in such episodes. This significant change is of interest, since the mixing of passive fields, such as chemical abundances or even active ingredients, such as magnetic fields (Tobias et al. 1998, 2001), may be influenced by these dramatic events. Such fields may be transported deeper than might be expected from time-averaged measures. It may even be possible that the majority of the transport of such quantities occurs in these rare events rather than by a gradual deposition via the more normal penetrative motions. Furthermore, even deeper and yet rarer events may exist that have not been picked up in the finite time histories of these simulations. It is intriguing to speculate whether, if one waited long enough, massive events may occur accomplishing the majority of the mixing and transport.

3.6. *Dependence on S*

We now examine the dependence of the overshooting convection on the parameters of the model. Of primary importance, is how the long-term influence of the overshooting, as measured by Δ_p, depends on the relative stability of the lower layer, S. A series of penetrative solutions are therefore presented with fixed Rayleigh and Prandtl numbers, $\mathrm{Ra} = 4.9 \times 10^5$ and $\mathrm{Pr} = 0.1$, but with varying stability ratios, $S = 0.5, 1, 2, 3, 7, 15, 30$ (cases 1–7).

Figure 8 shows the mean fluxes, $\langle F_k \rangle$, $\langle F_e \rangle$, $\langle F_c \rangle$, $\langle W_b \rangle$, and $\langle F_{\mathrm{ra}} \rangle$, for most of the cases mentioned above, and for $S = \infty$ (case 0). Here the label $S = \infty$ represents a nonpenetrative case, where a stress-free lower boundary is imposed at $z = 1$ (comparable to case 3 of Cattaneo et al. [1991] and case R0 of Brummell et al. [1996, 1998]). It should be noted that there is a significant difference between this case, where no stable layer exists, and the limit $S \rightarrow \infty$ in a penetrative case where a lower stable layer does exist, as demonstrated by Figure 8. In the nonpenetrative case, the boundary conditions at the lower edge of the domain enforce a heat flux, θ, that must remain fixed for all time. In the penetrative cases, while the background polytropic state is set up so that in hydrostatic balance the heat flux would have the same value θ at $z = 1$, as soon as motions set in this condition cannot be enforced. Similarly, $w = 0$ at $z = 1$ for all time in the nonpenetrative case, forcing the fluxes to vanish there. Figure 8 shows that the penetrative fluxes are not pinned to $z = 1$ and can choose a different form. Indeed, while overshooting always extends the positive profile of the kinetic flux $\langle F_k \rangle$ below the $z = 1$ interface, the remaining fluxes change sign either above or below $z = 1$ depending on S. In the penetrative cases, the deceleration of the downward motions is by buoyancy braking in the stable region rather than by the pressure effects of a lower impenetrable wall. The buoyancy work becomes negative at a depth that depends on the adjustments made to the background stratification. Since this depends on the relative stability of the layers, the point at which the buoyancy work becomes negative, and therefore the kinetic flux peaks and the other fluxes switch sign, is shallower for higher S. The nonpenetrative case is an anomaly, since less adjustment of the mean stratification is possible, and the downflow motions are decelerated by the wall rather than by buoyancy braking, leading to no changes in sign of the fluxes in the interior of the convective region. For $S = \infty$, the zeroes of the other fluxes are necessarily tied to the zero of the kinetic flux, rather than its peak, as is the case for penetrative motions. Even as S becomes large, it is not clear that the $S = \infty$ case will be recovered, since some interaction with the lower stable region is always allowed, even if it is in the form of gravity waves.

A corollary of these observations is that an understanding of the dynamics of a convection zone built on the intuition of the $S = \infty$ case may lead to a false sense of the depth of the zone. When a strongly stable lower layer is present, the convection zone (as it might intuitively be defined on the fluxes other than the kinetic flux) appears to be compressed into a shallower layer than might be expected. This counterintuitive feature is also realized in the more common definition of the convection zone depth based on the entropy gradient (see Fig. 10, discussed in detail shortly).

Returning to the main topic, Figure 8 clearly exhibits a variation of the kinetic flux profile with S and therefore a dependence of the penetration depth with S. Figure 9 summarizes this dependence by showing the values of Δ_p versus S gleaned from the primary set of simulations. The error bars for each point indicate the rms error induced by the fluctuations in the time averaging for each simulation. As S is increased over the range $0.5 \leq S \leq 30$, the penetration depth Δ_p generally decreases. This implies that the more stable the lower layer, the less the overshooting penetrates into that layer. This general trend is expected, since raising S steepens the density and entropy gradients in the stable layer, thereby decreasing the downward buoyancy driving of a fluid element entering the overshoot region, and thus providing an increased resistance (or buoyancy braking) to penetrating motions. For the range of S studied, the average overshooting is between $0.28 \leq \Delta_p \leq 0.94$, measured in units of the convection zone depth, and roughly twice as much in units of the pressure scale height.

Two scaling law lines are added to Figure 9, drawn as dotted lines, representing lines where Δ_p is proportional to $S^{-1/4}$ and S^{-1}. These scaling laws arise from the modeling presented in Hurlburt et al. (1994). In that paper, it is proposed analytically, and confirmed with two-dimensional numerical simulations, that two regimes of scaling with S

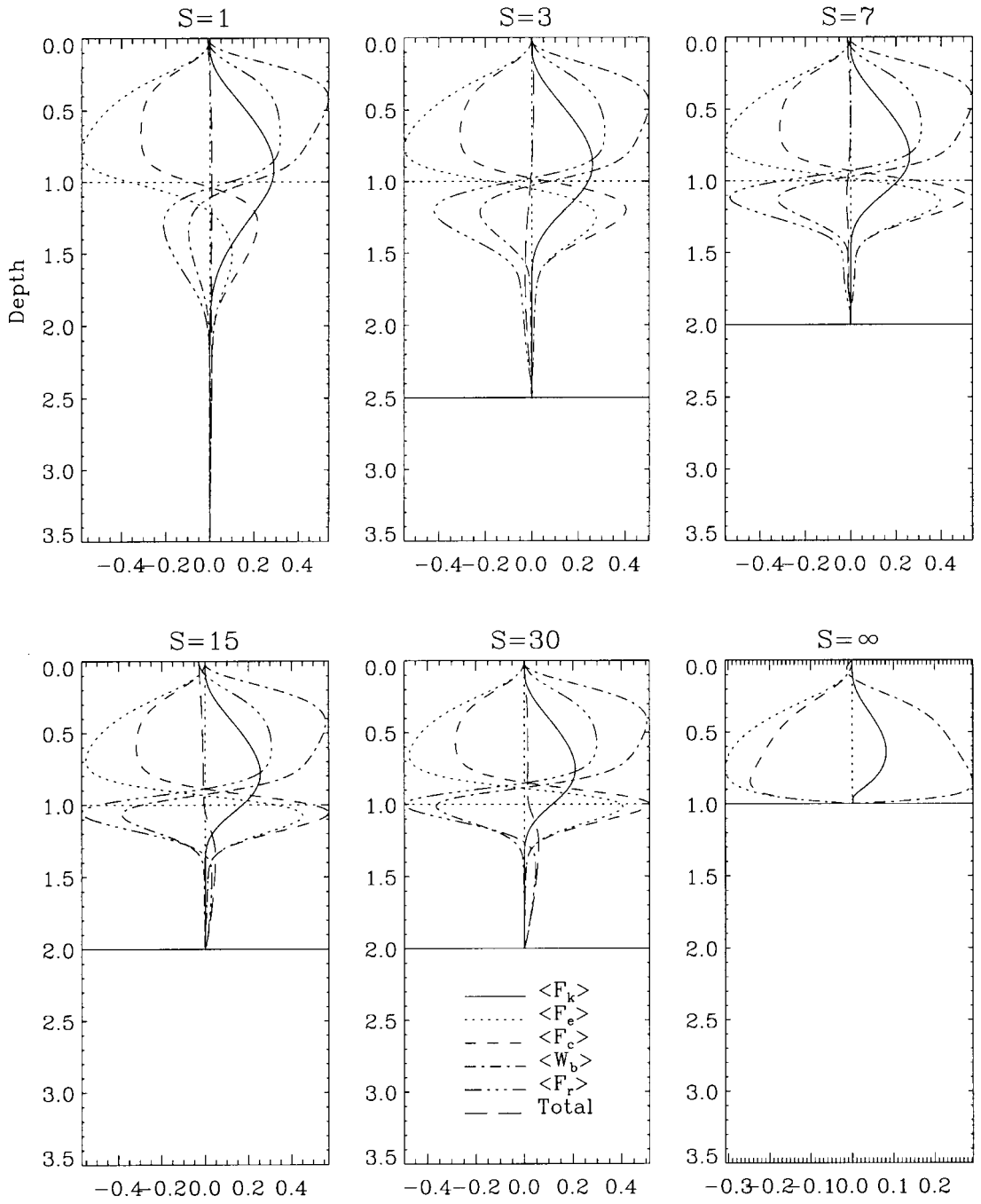

FIG. 8.—Mean fluxes for different values of S (cases 2–7 and 0). Each value of S exhibits the mean kinetic flux $\langle F_k \rangle$ (*solid line*), the enthalpy flux $\langle F_e \rangle$ (*dotted line*), the total convective flux $\langle F_c \rangle = \langle F_k + F_e \rangle$ (*dashed line*), the buoyancy work $\langle W_b \rangle$ (*single-dot–dashed line*), the adjusted radiative flux $\langle F_{\rm ra} \rangle = \langle F_r \rangle - C_k \theta \gamma / (\gamma - 1)$ (*triple–dot–dashed line*), and the adjusted total flux (neglecting viscous effects) $\langle F_T \rangle = \langle F_c + F_{\rm ra} \rangle$ (*long-dashed line*).

exist. At lower S, where the unstable layer is more pliable, motions penetrate and mix their thermodynamic properties efficiently just below the interface, creating a *nearly adiabatic region* there. This then matches to the deeper underlying quiescent stable layer through a *thermal adjustment region*. The calculations of Hurlburt et al. (1994) show that a scaling of S^{-1} may be associated with the presence (and dominance) of the nearly adiabatic region which occurs at lower S, whereas for stiffer lower layers (higher S), that region is suppressed and the existence of solely the thermal adjustment region leads to a scaling of $S^{-1/4}$. These scaling laws were also later seen in the three-dimensional work of Singh et al. (1995).

Figure 9 indicates that the measured Δ_p in the primary sequence of turbulent simulations carried out in this study (cases 1–7) appear to be roughly consistent with a scaling law of $S^{-1/4}$ for all S. No strong evidence for S^{-1} regime even at low S is exhibited. Judging from the results of Hurlburt et al. (1994), this would imply that there is very little real penetration in this highly nonlinear three-dimensional problem and only overshooting. In other words, although motions continue below the interface, there is no extension of the well-mixed adiabatic interior of the convection zone into the stable region.

This can be confirmed by examining the mean entropy gradient profiles for our range of S, shown in Figure 10. As

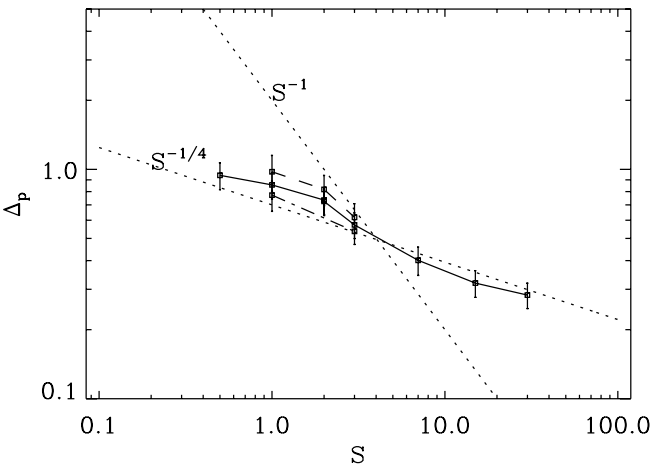

FIG. 9.—Dependence of the penetration and overshooting measure Δ_p on S. The solid line joins values of Δ_p for varying S at the benchmark parameters (cases 1–7). In this and subsequent plots of Δ_p, error bars are shown representing the rms fluctuations around the mean value of Δ_p. The dashed line shows the scaling of some solutions at low R_a (cases 23, 22, and 16), while the dot-dashed line shows the result for some high P_e solutions for low S (cases 24 and 17). Scaling laws for S^{-1} and $S^{-1/4}$ are shown as dotted lines.

mentioned earlier in reference to Figure 2*d*, the entropy gradient profile in the convection zone generally consists of a strong driving superadiabatic gradient near the upper boundary and an adiabatic interior, where the entropy has been homogenized by the convective mixing. This interior must then be matched to the negative entropy gradient of the lower stable layer via a transition region surrounding the interface at $z = 1$. The jump in entropy in this region is related to the stability of the lower layer and obviously is larger for the high S (more stable, very subadiabatic) lower layers. At the lower, more pliable S ($S = 0.5,\ 1,\ 2,\ 3$), however, just below the interface the entropy gradient adjusts toward a more isentropic (zero entropy gradient) profile again over a small region, before matching to the required entropy gradient below. It was such a region—this "bump" returning toward zero in the entropy gradient profile—that Hurlburt et al. (1994) identified as the nearly adiabatic region responsible for the S^{-1} dependence. We see here that this effect is distinctly less pronounced in these three-dimensional simulations than it was in their two-dimensional calculations. At these parameters, very little return to adiabaticity is seen in the stable region, even at low S, and thus the S^{-1} scaling is not seen.

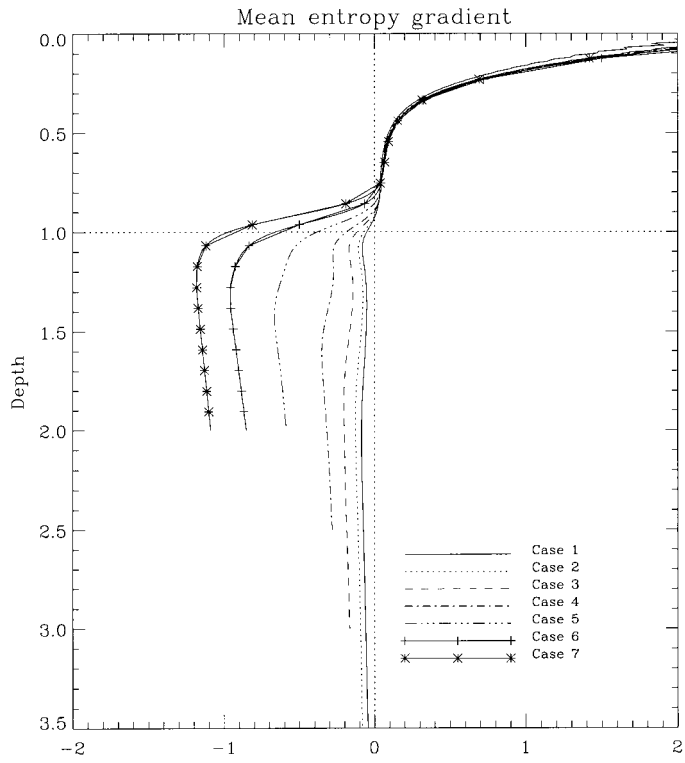

FIG. 10.—Time- and horizontally averaged entropy gradient as a function of S (cases 1–7).

The explanation for this is most likely that these simulations are of *turbulent three-dimensional* convection and therefore have significantly different structure from *laminar* and *two-dimensional* situations. The nature of the three-dimensional penetration is that strong downflowing plumes span the convection zone and penetrate out of the driving region into the stable layer. Away from the upper boundary, these structures are isolated regions and have a low filling factor, i.e., the area covered at any depth by such entities is a small percentage of the total area (10%–20% at $z = 1$). Their ability to mix and homogenize the mean thermal variables below the interface is therefore weak. The two-dimensional simulations of Hurlburt et al. (1994) did exhibit plumelike behavior, but these induced significant roll-like vortex overturnings that intruded below the interface. The plumes in these two-dimensional simulations are also necessarily infinite sheets with a larger planform filling factor than the true three-dimensional structures. These two effects combined provide an efficient homogenization of the thermal structure down to the lowest extent of the extended motions.

The three-dimensional simulations of Singh et al. (1995) are not greatly turbulent and are not dominated by plumelike penetration, possibly explaining why their results concur with those of the two-dimensional simulations. To test this hypothesis out somewhat, Figure 9 also shows a dashed line representing the variation of the penetration depth, Δ_p, with S at low S for some lower Rayleigh number calculations (cases 23, 22, and 16). These points correspond to simulations with $\mathrm{Ra} = 5 \times 10^4, \mathrm{Pr} = 0.1$ for $S = 1,\ 2$ and $\mathrm{Ra} = 10^5, \mathrm{Pr} = 0.1$ for $S = 3$. These more laminar simulations do have overturnings that are more cellular in nature, which engender a larger filling factor around the interface (>20%), but the penetration depths still do not fit an S^{-1} dependence well. This seems to imply that it is not purely the structure of the convection that is responsible for the nonexistence of the nearly adiabatic region, but that some other mechanism is also at work. We suspect that the Péclet number may play an important role, and therefore proceed to examine the effect of this parameter.

3.7. *Effect of the Péclet Number*

Despite the increasing level of computational resources, these models necessarily operate at parameters far removed from their astrophysical values. For example, the Rayleigh and Reynolds numbers in these calculations are many orders of magnitude lower than the astrophysical estimates, while the Prandtl number is too large (e.g., compare values in Table 2 to the estimated astrophysical values of

TABLE 2

MEASURED PARAMETERS FOR THE COMPRESSIBLE PENETRATIVE CONVECTION SIMULATIONS

	REYNOLDS NUMBERS (Re)						VERTICAL VELOCITY, w_{rms}				PÉCLET NUMBERS (Pe)	
	u_{rms}		u_{max}		λ		cz Full		cz Down		u_{rms}	
CASE	Tot	cz	Tot	cz	Tot	cz	Max	$z = 1$	Max	$z = 1$	Full	Down
0.....	416	411	1157	1142	41.1	40.7	0.27	...	0.32	...	...	...
1.....	334	319	1870	1267	4.3	3.9	0.30	0.24	0.45	0.39	218	49.0
2.....	337	341	1855	1388	4.2	4.0	0.32	0.25	0.48	0.41	229	48.3
3.....	339	319	1769	1293	5.5	5.5	0.33	0.27	0.51	0.44	218	42.5
4.....	314	298	1636	1200	6.5	7.8	0.32	0.25	0.49	0.42	198	36.0
5.....	315	320	1627	1320	8.8	10.8	0.33	0.23	0.49	0.37	196	27.4
6.....	286	321	1525	1386	7.8	10.4	0.33	0.21	0.50	0.34	186	17.9
7.....	241	290	1286	1230	6.7	9.8	0.31	0.17	0.46	0.27	153	9.5
(5)	315	320	1627	1320	8.8	10.8	0.33	0.23	0.49	0.37	196	27.4
8.....	296	323	1488	1307	9.0	14.5	0.33	0.21	0.48	0.34	185	47.7
9.....	276	286	1007	1026	15.2	9.9	0.29	0.14	0.33	0.18	112	36.6
10.....	319	294	1066	1025	11.2	16.5	0.30	0.15	0.32	0.17	112	36.8
11.....	335	391	1304	1380	10.7	12.4	0.37	0.17	0.43	0.20	130	23.8
12.....	329	360	1249	1307	10.4	10.8	0.33	0.16	0.40	0.19	122	24.8
13.....	296	284	945	979	11.6	9.1	0.27	0.12	0.31	0.14	88	19.7
14.....	308	284	1019	1025	11.5	8.9	0.27	0.12	0.32	0.15	94	19.9
15.....	290	261	981	929	15.4	9.2	0.27	0.12	0.30	0.15	93	18.8
(9)	276	286	1007	1026	15.2	9.9	0.29	0.14	0.33	0.18	112	36.6
16.....	147	149	745	545	3.9	5.0	0.37	0.28	0.54	0.48	97	17.0
(4)	314	298	1636	1200	6.5	7.8	0.32	0.25	0.49	0.42	198	36.0
17.....	402	413	2108	1744	7.3	8.0	0.33	0.24	0.48	0.38	258	47.4
18.....	715	785	3935	3748	11.2	9.5	0.28	0.19	0.43	0.30	470	88.2
19.....	974	1062	5088	5276	13.8	11.2	0.28	0.17	0.41	0.26	582	113.8
20.....	2010	2220	10062	11514	26.8	19.0	0.28	0.15	0.41	0.22	726	144.7
21.....	1655	1795	8384	9830	20.9	13.0	0.25	0.13	0.37	0.20	922	184.2
22.....	119	119	612	420	2.5	3.2	0.39	0.32	0.58	0.54	80	14.8
(3)	339	319	1769	1293	5.5	5.5	0.33	0.27	0.51	0.44	218	42.5
23.....	124	123	670	425	2.1	2.5	0.37	0.30	0.54	0.51	86	17.4
(2)	337	341	1855	1388	4.2	4.0	0.32	0.25	0.48	0.41	229	48.3
24.....	451	455	2432	1976	4.9	4.1	0.32	0.23	0.47	0.38	297	62.7
(17)	402	413	2108	1744	7.3	8.0	0.33	0.24	0.48	0.38	258	47.4
25.....	617	648	3298	2672	9.6	10.8	0.35	0.26	0.52	0.41	200	37.3
(4)	314	298	1636	1200	6.5	7.8	0.32	0.25	0.49	0.42	198	36.0
(25)	617	648	3298	2672	9.6	10.8	0.35	0.26	0.52	0.41	200	37.3
26.....	1258	1350	6699	5564	15.1	14.9	0.37	0.27	0.52	0.41	206	39.3

NOTE.—Here u_{rms} and u_{max} imply that a quantity has been created using either the rms value of the velocity or the maximum velocity value, respectively, and λ implies that the quantity is the Taylor microscale value. The label "Tot" implies that the quantity was calculated as an average of the whole domain, whereas "cz" implies that it was calculated only over the convection zone. The column header "Full" implies that both upflows and downflows were included in the average, whereas "Down" means that only downflows were used. The measure of the vertical velocity is given both as the maximum of its space- and time-averaged profile in z (denoted by "Max") and as its value at the base of the convection zone (denoted by $z = 1$). Case 20 is only marginally resolved, probably leading to some of the unexpected table entries.

$\mathrm{Re} \geq 10^{12}, \mathrm{Pr} < 10^{-8}$). It may also be expected that the related Péclet number is very low in these simulations compared to astrophysical values. It has been suggested (J.-P. Zahn 2001, private communication) that raising the Péclet number to emphasize advective effects over thermal diffusion may lead to a more astrophysical view of the penetration and a possible return to the two-dimensional scaling. We note that the two-dimensional simulations can often attain artificially high Péclet and Reynolds numbers since the lack of the third degree of freedom forces the cellular motions into fast, flywheeling overturning motions, artificially raising the rms velocity substantially (see also Muthsam et al. 1995). Furthermore, models such of those of Singh et al. (1995), where the only diffusive mechanisms in the problem are numerical rather than physical, can also have an artificially high effective Péclet number (depending on the numerical grid size).

Our last sequence of simulations examined above (cases 23, 22, and 16) lowered Ra for fixed Pr, and thus actually lowered the Péclet number. We therefore now investigate the effect of increasing the Péclet number by decreasing C_k at fixed Prandtl number (and thereby increasing Ra) over a series of simulations at $S = 3$ (cases 16–21). We chose $S = 3$ since it was the stiffest stable layer that exhibited the slight return toward adiabaticity just below the unstable-stable interface: a stiff calculation is both more computationally efficient and more likely representative of the transition between the solar convection zone and the tachocline. In this series of simulations, C_k is reduced over the range $0.15 \geq C_k \geq 0.0077$, so that $1 \times 10^5 \leq \mathrm{Ra} \leq 4 \times 10^7$. Maintaining constant Pr means that the viscosity is also reduced, and this contributes to the associated increase in measured Reynolds numbers (see Table 2). The Péclet number can be measured in an assortment of ways depending on the choice

of the characteristic velocity, U, and length scale, l, as for the Reynolds number. Table 2 exhibits two Péclet numbers each evaluated at the base of the convective layer, $z = 1$. One, denoted by $\mathrm{Pe}_{\mathrm{tot}}$, is based on the rms velocity and the depth of the convection zone (unity). The other, $\mathrm{Pe}_{\mathrm{down}}$, is based on the rms velocity in the downflows only and a length scale of the downflows, calculated by taking the square root of the fractional area that they occupy. Most theories of plume penetration (Schmitt et al. 1984; Hurlburt et al. 1994) use the latter characteristic quantities to evaluate the penetration. For this set of simulations, $97 \leq \mathrm{Pe}_{\mathrm{down}} \leq 922$ and $17 \leq \mathrm{Pe}_{\mathrm{tot}} \leq 184$, exhibiting an order-of-magnitude variation over the series of simulations. The Péclet numbers can be significantly higher in the convection zone where the kinetic flux peaks, and drop off in the stable region as the velocities reduce there. This variation of parameters then appears to provide one route toward more astrophysical values as desired. However, this path through parameter space is not the only choice with the desired properties, and others are discussed presently.

Figure 11 shows qualitatively what a high Péclet number solution looks like. The case shown (case 20) has $\mathrm{Ra} = 2 \times 10^7$ ($C_k = 0.011$). Immediately apparent in the volume renderings is the increased complexity of the flow. The greater degree of nonlinearity has decreased the cellular spacing between the downflows (Fig. 11*a*) and thus reduced the distance between plumes in the enstrophy density field (Fig. 11*b*). The downflows and vortical structures are also all narrower because of the reduction in the thermal and viscous diffusivities (both have reduced compared to case 4 since the Prandtl number was kept constant at $\mathrm{Pr} = 0.1$). This is further evident in the enstrophy density rendering as a substantial increase in small-scale turbulence associated with the base of plumes. This effect is probably enhanced by stronger buoyancy braking in the stable region due to the slower thermal diffusion time associated with the plumes.

We now examine quantitatively whether these higher Péclet number simulations and their apparent increased levels of turbulence lead to stronger thermodynamic mixing in the stable layer due to the effects observed above. Figure 12 exhibits the entropy gradient for the series of simulations run with varying C_k at fixed Pr for $S = 3$ (cases 16, 4,17, 18,20, and 21). The interior of the convection zone ($0 \leq z \leq 1$) becomes much closer to adiabatic as C_k decreases, indicating that the convection operates more efficiently at the higher Pe. This may be expected since this variation of parameters means that the Rayleigh number increases, implying that the convection is more supercritical, or in other words, more strongly forced. It is noteworthy that in these three-dimensional simulations it is necessary to go to much higher Ra than in the two-dimensional simulations of Hurlburt et al. (1994) in order to establish this well-mixed interior convective flow. The two-dimensional entropy profiles showed highly isentropic interiors at $\mathrm{Ra} = 10^5$, whereas these three-dimensional simulations require more than $\mathrm{Ra} = 2 \times 10^7$ for a similar profile. This adds further evidence to the notion that the topology of three-dimensional compressible penetrative convection is not as connected as the two-dimensional motions, in the sense that the return upflows are not driven as directly by the downflows.

In Figure 12 the end of the relatively well-mixed region occurs around $z = 0.9$. Empirically, this point seems relatively independent of C_k, as is the entropy gradient in the deep stable region ($z \geq 1.5$) by construction. However, the transition region between the upper adiabatic region and the deep profile is strongly dependent on the Péclet number. At lower Pe (higher C_k, lower Ra [e.g., case 16]), the transition to a value close to the deep stable layer occurs abruptly, over a depth of roughly 0.2 units. A small reverse trend toward a more adiabatic profile then occurs as mentioned previously, reminiscent of the nearly adiabatic region in Hurlburt et al. (1994). As Pe is increased, the trend is *not* to make this reverse "bump" more nearly adiabatic, but instead to form a less abrupt transition region. Instead, the adiabatic convection zone becomes linked to the deep stable interior gradient by a smooth, almost linear ramp in the entropy gradient. While it is true that points in the transition zone become generally closer to the adiabatic value as the Pe number is increased, the region is not an isentropic plateau encroaching upon adiabaticity. Although the decreased diffusivity for the higher Pe cases allows the downflowing plumes to retain their thermal content more readily in the overshoot region, the low filling factor of the plumes still does not permit sufficient mixing to make the zone adiabatic. For all parameter values evaluated in these studies, even the highest Pe, the overshoot zone appears more like an adjustment region. This bodes badly for a S^{-1} scaling law that demands an extended adiabatic region even at high Pe, favoring the existence of the thermal adjustment $S^{-1/4}$ law.

The penetration depth Δ_p decreases with increasing Pe (as shown by the values given in Table 1 and on Fig. 12). One might expect this result to stem from a competition between increased buoyancy braking in the stable region due to the decreased C_k (acting to lower Δ_p) and enhanced vertical velocities due to the higher supercriticality with higher Ra (raising Δ_p). However, another factor arises, owing to the nature of the penetrative model, that appears to dominate. This is the fact that reducing C_k implies a reduction of the energy flux [$= C_k \theta \gamma / (\gamma - 1)$] supplied to the system. This leads to a reduction in the actual rms downflow velocities with increasing Pe (Fig. 13*a*), rather than the expected increase at the higher Pe and Ra. Furthermore, since the viscosity is decreasing to match the decrease in C_k in order to keep Pr fixed, the filling factor f of the strong downflows at the base of the unstable region is also decreasing (Fig. 13*b*), although the total downflows are increasing in area slightly. The slower downflow velocities and their decreased filling factor will both tend to decrease the overshooting depth.

The measured scaling of Δ_p with Pe here, shown in Figure 14, is less drastic than the $f^{1/2} w^{3/2}$ (measured at $z = 1$) law predicted by the models of Schmitt et al. (1984). This deviation was anticipated by Hurlburt et al. (1994). The decrease in penetration depth with increasing Péclet number shows no sign of tailing off at high Péclet numbers: the last four points in the figure are suggestive of a scaling law of $\Delta_p \sim \mathrm{Pe}^{-1/2}$ (*dashed line*; the best fit is $\mathrm{Pe}^{-0.46}$), although the data is not sufficient to be truly convincing. It is perhaps also instructive to examine the scaling directly with C_k to eliminate the effects of the downflow velocity and filling factor. Figure 15 exhibits that a scaling of $\Delta_p \sim C_k^{1/3}$ fits the lower C_k portion of the curve reasonably well (the best-fit line to the last three points has exponent 0.30). This is considerably less steep than one might expect from purely a reduction of the input energy flux.

The form of the entropy profiles (Fig. 10) seems to indicate that the nearly adiabatic region of Hurlburt et al.

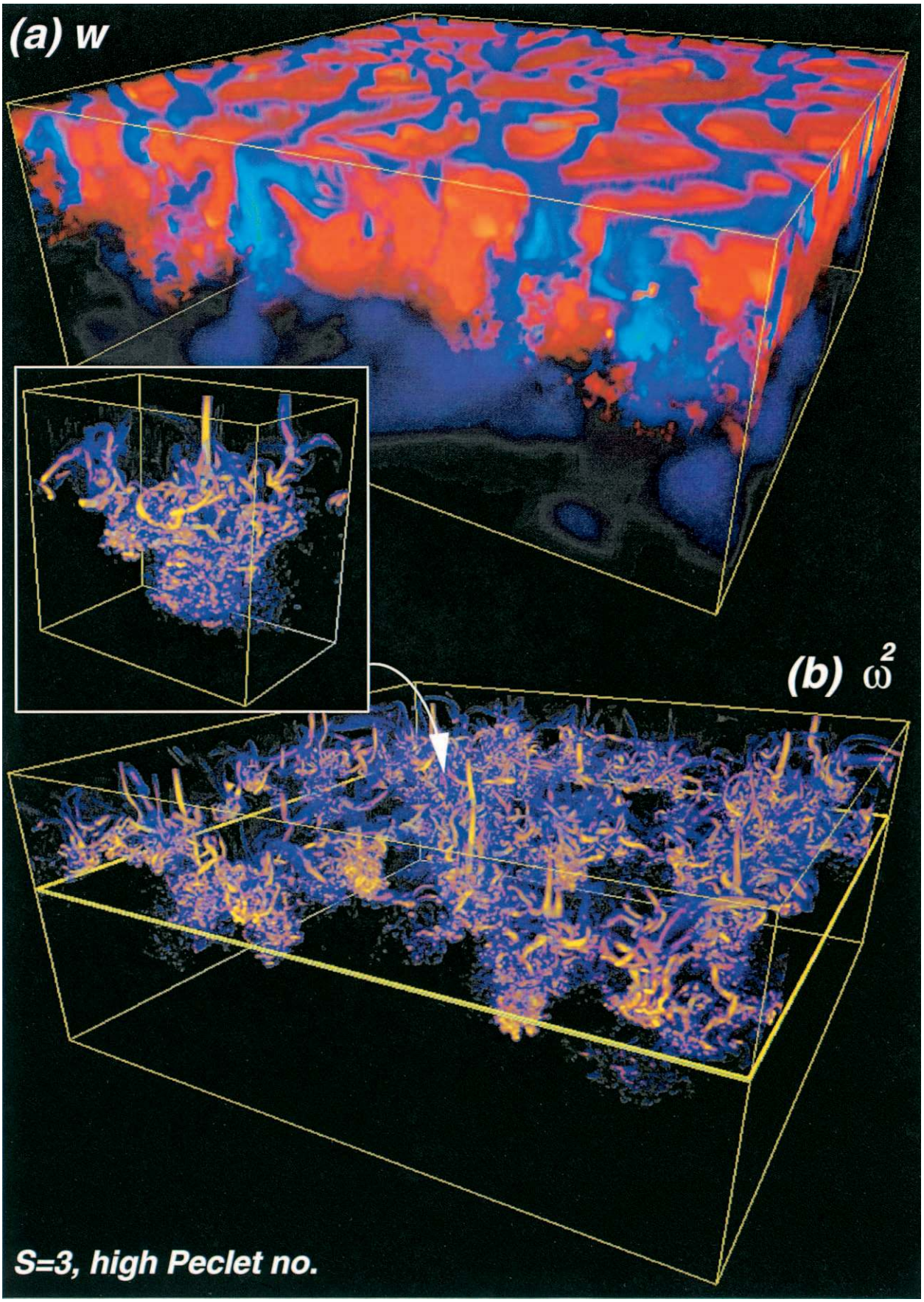

FIG. 11.—Example volume renderings from a representative time of (*a*) the vertical velocity w and (*b*) enstrophy density ω^2 for a high Péclet number solution (case 21). This solution lowers C_k to $C_k = 0.0077$, leading to a Rayleigh number of $R_a = 4 \times 10^7$ and a Péclet number for the downflows of about 185. The inset shows details of a downflow. The data resolution had to be downsized for visualization purposes.

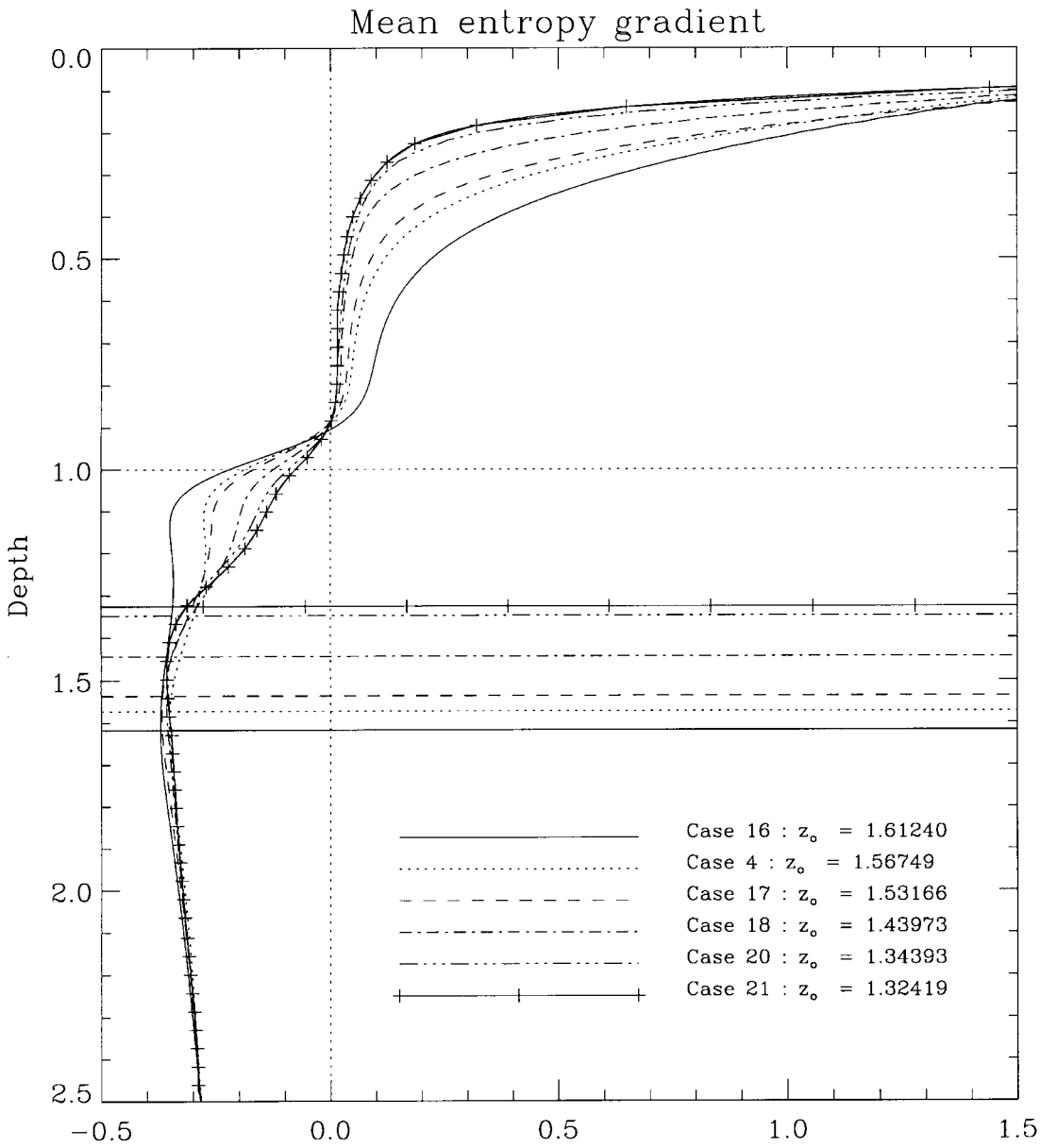

FIG. 12.—Variation of the time- and horizontally averaged entropy gradient with the Péclet number for $S = 3$ (cases 16, 4, 17, 18, 20, and 21). Horizontal lines in styles corresponding to the cases and the annotations to the key show the overshooting depths z_o measured for each case.

(1994) is not being recovered even at high Pe. However, the reduction of Δ_p with increasing Pe at one point ($S = 3$), while suggestive of a flattening away from S^{-1} rather than a steepening toward it, is insufficient to infer the scaling with S at high Péclet number. Therefore, a further high Pe calculation was conducted at $S = 1$ with $C_k = 0.5$ and $\mathrm{Pr} = 0.1$ ($\mathrm{Ra} = 10^6$ [case 24]), for comparison with case 17. The penetration depths Δ_p for these calculations are included on Figure 9 as the dot-dashed line. These two points minimally suggest that the S dependence is much less steep than S^{-1}, seemingly again much closer to the $S^{-1/4}$ dependence related to a thermal adjustment region.

3.8. *Other Parameter Routes to Higher Reynolds Numbers*

It is of course possible to traverse other routes through parameter space toward more astrophysical values, for example, by decreasing the Prandtl number either at fixed Rayleigh number or at fixed C_k. The former path requires $\mathrm{Pr}\, C_k^2$ fixed and therefore an increasing C_k as Pr decreases. In this case, both the viscosity must decrease and the input energy flux increase. On the second path where the Prandtl number is decreased for fixed C_k, the input energy flux is fixed, and we are solely varying the viscosity of the fluid (a course previously followed in Cattaneo et al. 1991; Brummell et al. 1996, 1998, for example). Alternately, we could increase Ra and decrease Pr at the same rate in order to operate at fixed viscosity, thereby varying C_k independently (although now the input energy flux varies too). While convection is technically governed by the dimensionless ratios of parameters that we are working with, it is sometimes beneficial to consider the underlying physical parameters varying individually. We have therefore performed two further simulations at $S = 3$ to exhibit the trends associated with at least the first two of these different paths. Cases 17 and 25 follow the first track (fixed $\mathrm{Ra} = 10^6$, $\mathrm{Pr} = 0.1, 0.5$, giving

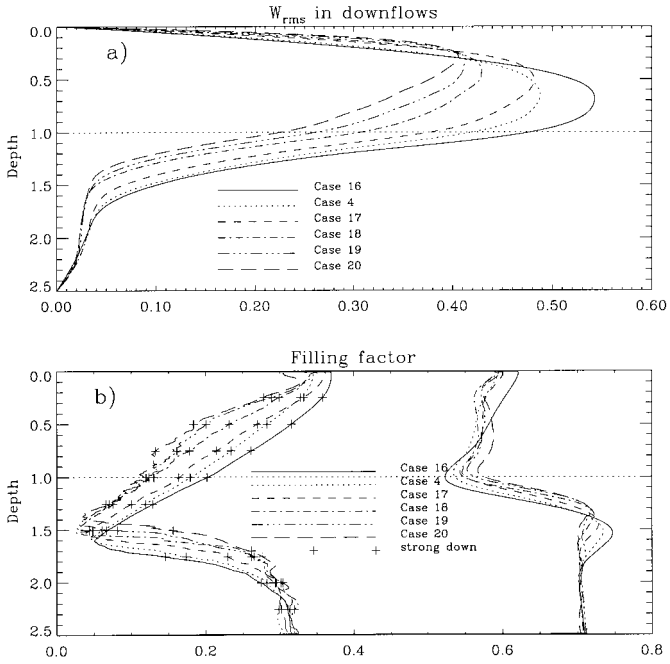

FIG. 13.—Variation of (*a*) the rms vertical velocity and (*b*) the filling factors of the downflows (*lines without crosses*) and strong downflows (*lines with crosses*) with depth, for various cases at $S = 3$ with different Péclet numbers (cases 16, 4, 17, 18, 19, and 20).

$C_k = 0.05, 0.07$), whereas cases 4, 25, and 26 follow the second (fixed $C_k = 0.07$, $\mathrm{Pr} = 0.1, 0.5, 0.25$, giving $4.9 \times 10^5 \leq \mathrm{Ra} \leq 2 \times 10^6$). We have not studied the third route where solely C_k changes, since then the input energy flux would change between simulations unless theta was adjusted for each case. If that were done, the underlying polytrope for each case would be different and the results would be difficult to compare.

Table 2 indicates that both paths lead to increased measures of the Reynolds numbers as expected. At fixed C_k, the

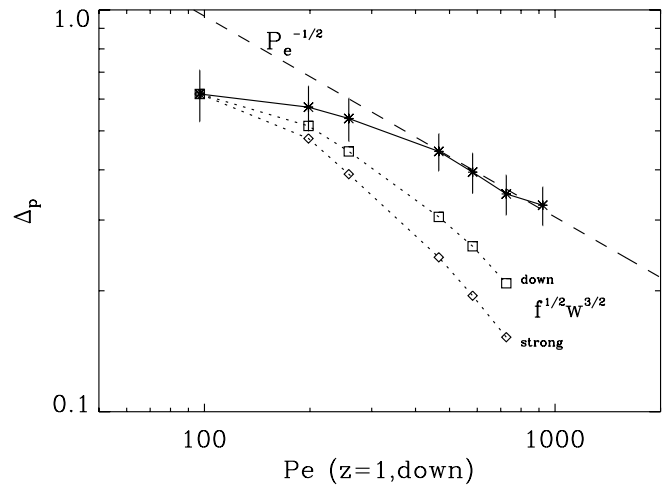

FIG. 14.—Variation of the penetration and overshooting measure Δ_p with the Péclet number, for cases at $S = 3$ (cases 16, 4, 17, 18, 19, and 20). Also plotted is the scaling suggested by the arguments of Schmitt et al. (1984) and Zahn (1991) in terms of the filling factor and the plume velocity of exit from the base of the convection zone. These scalings are shown for both the full downflow field and the strong downflow field (representative of the plumes) only. A further scaling line (*dashed line*) is plotted that fits the three highest Péclet number points well.

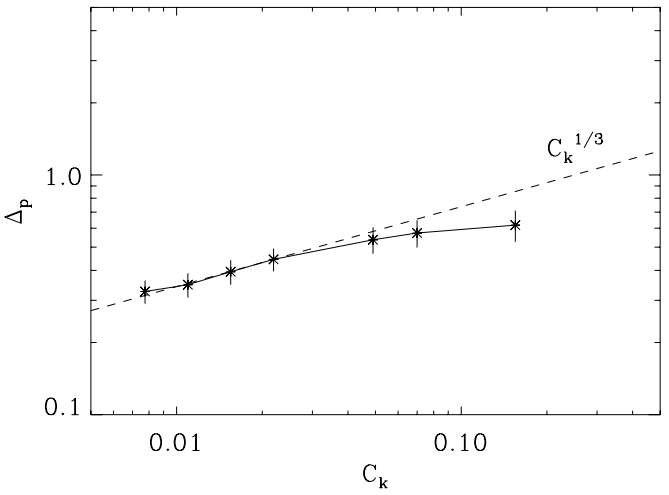

FIG. 15.—Variation of the penetration and overshooting measure Δ_p directly against C_k. A scaling line (*dashed line*) fitting the last three points is added.

rising value appears to be purely due to the reduced viscosity, as indicated by the close scaling of the measures with Pr. For fixed Ra, the increased energy flux also contributes to an increased Re. The penetration depth Δ_p for the fixed Ra cases appears to increase slightly from $\Delta_p = 0.537$ to $\Delta_p = 0.555$ (although the margin of error in these measurements is about 0.01). This effect is associated with the increase in the downflow velocities (Fig. 16*a*) created by the reduction of the viscosity and the increase in input energy flux. For the cases at fixed C_k, with only the viscosity decreasing, one might expect a slightly increased penetration depth again due to the decreased diffusion of the motions. However, Table 2 shows that decreasing the Prandtl number in this manner leads to a small but significant decrease in the penetration depth, from $\Delta_p = 0.57$ for $\mathrm{Pr} = 0.1$ to $\Delta_p = 0.54$ for $\mathrm{Pr} = 0.025$. This corresponds to roughly a 6% decrease in penetration depth with a fourfold decrease in the Prandtl number, with a best fit to this data suggesting a weak dependence like $\Delta_p \sim \mathrm{Pr}^{0.05}$. Figure 16*c* shows that the rms vertical velocities in the downflows did indeed increase in the convection zone as expected with the lower Prandtl number but are very similar in value in the stable region. One might expect the penetration depth to remain the same then, with similar velocities and the same thermal diffusivity, but the filling factor plays a role too. At the lower viscosity, the velocity structures are narrower and so the filling factor of the strong downflows at the interface decreases a little (Fig. 16*d*). It is this then that leads to the decrease in penetration depth. The decrease in downflow velocity in the stable region with the reduction in viscosity may be due to shear instabilities and entrainment in the higher speed plumes in combination with the geometric effects described above.

We tentatively conclude from this small amount of evidence that the dependence of penetration on the Prandtl number is only weak. When the viscosity is most significantly effected by the changing Prandtl number (i.e., at fixed C_k, $\mu \sim \mathrm{Pr}$), the penetration depth is controlled more by the filling factor than any velocity changes. For fixed Ra, the effect of changing Pr on the viscosity is weaker ($\mu \sim P_r^{1/2}$), and therefore the filling factor is little affected, but the velocities are raised by the raising of the input energy flux with

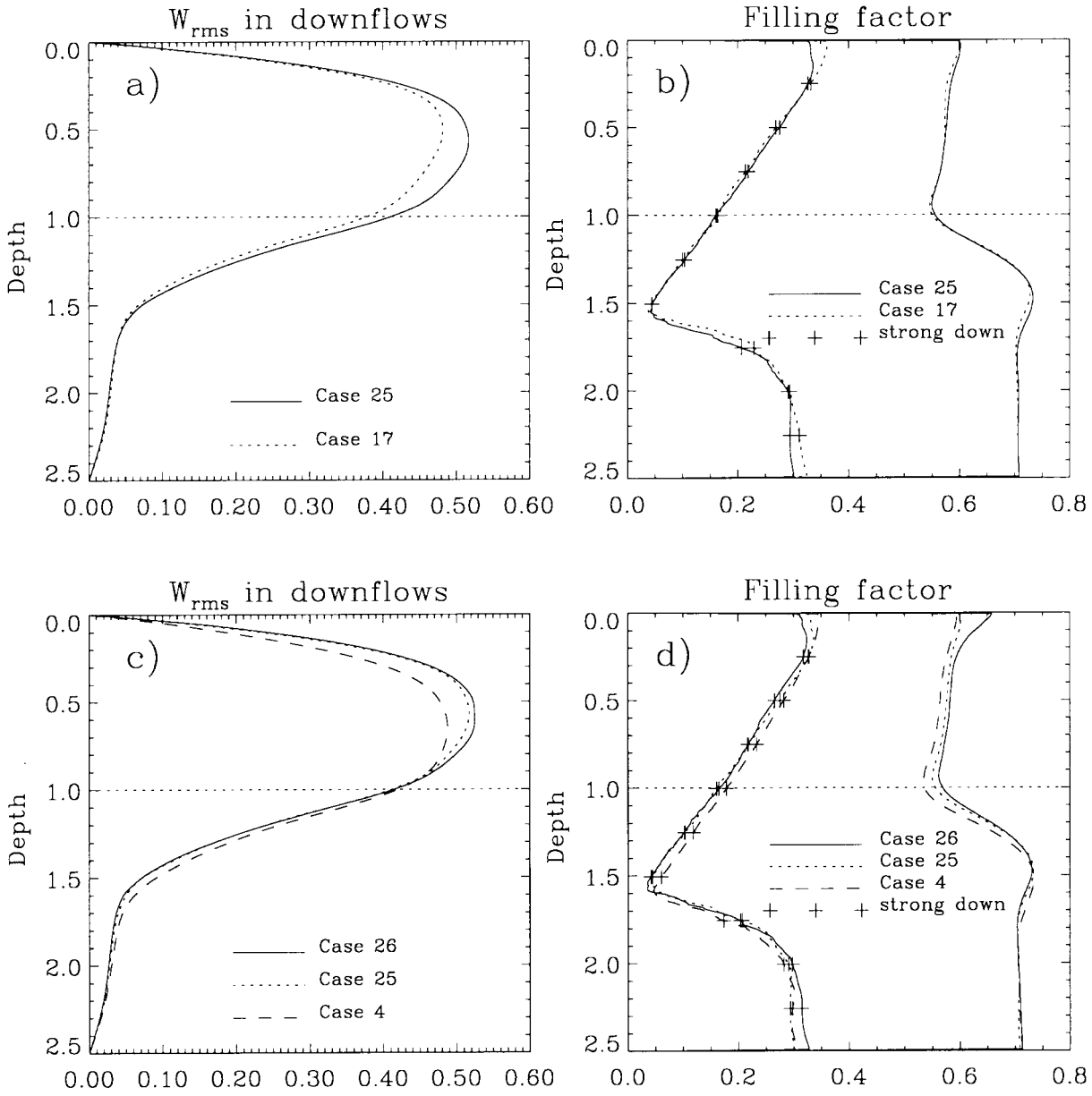

FIG. 16.—Variation of the rms vertical velocity and the filling factor of the downflows and strong downflows (similar to Fig. 13) along other routes to more astrophysical parameters with $S = 3$. Rather than varying C_k at fixed Pr as in previous plots, these plots show the effects of varying Pr with either fixed Ra (*a* and *b* [cases 25 and 17]) or fixed C_k (*c* and *d* [cases 26, 25, and 4]).

C_k. However, keeping θ fixed so that raising C_k raises the input energy flux is somewhat artificial in the astrophysical context, and without this effect we might expect a slight reduction of the penetration depth in this case too. Extrapolation of these results directly to the situation of the tachocline is unwise. However, the indications are that the deep penetration exhibited in these simulations (a significant fraction of the scale height) might be eroded somewhat at parameters more representative of the solar context.

4. PENETRATIVE CONVECTION WITH ROTATION

Since most stars and planets rotate, the influence of rotation on the overshooting mechanisms described above is also of fundamental interest. Although the Sun is not a fast rotating body, on the larger scales of motion the Coriolis force will certainly be felt. Supergranules are the smallest motions that might be expected to have some weak influence from the rotation. Motions on the order of the convection zone depth (200 Mm) like the proposed (but hard to detect) giant cells will possess a Rossby number approaching unity, where their overturning timescale is comparable to the rotation period, and therefore they will certainly be influenced. In the gas giant planets, such as Jupiter, the faster rotation will influence many scales of motion.

Here we systematically investigate the influence of rotation, included via an *f*-plane formulation in the model, on the overshooting characteristics of penetrative convection. A number of simulations were run based around the $S = 7$ benchmark simulation, extending it to various rotation rates (Ta) and latitudes (ϕ), for fixed values of the other parameters. It has been a long-standing open question (see,

e.g., Julien et al. 1996a) as to what the influence of rotation is on overshooting convection, and we attempt to answer that here for turbulent compressible convection.

4.1. *Overview of Motions with Rotation*

Investigations of turbulent rotating compressible convection (Brummell et al. 1996, 1998) have already exhibited and explained changes in turbulent convective topology due to a rotational influence. Most notably, while the small-scale turbulent motions decouple from the effects of rotation (since they overturn too quickly to feel the Coriolis force), the spatially and temporally coherent downflow structures can become aligned with the axis of rotation. Although the coherent structures are retained in the penetrative version of the problem, we have found that the presence of the stable region changes the characteristics of the convection somewhat. We therefore here investigate whether this turbulent rotational alignment remains in the penetrative case and describe the properties of the penetrative motions in the presence of rotation.

Figure 17 exhibits the nature of rotating penetrative convection as compared to an equivalent case that is not rotating (case 10 compared to case 5). The rotation here is parallel to gravity (i.e., $\phi = 90°$) and is the fastest rotation rate simulated, corresponding to a Rossby number,

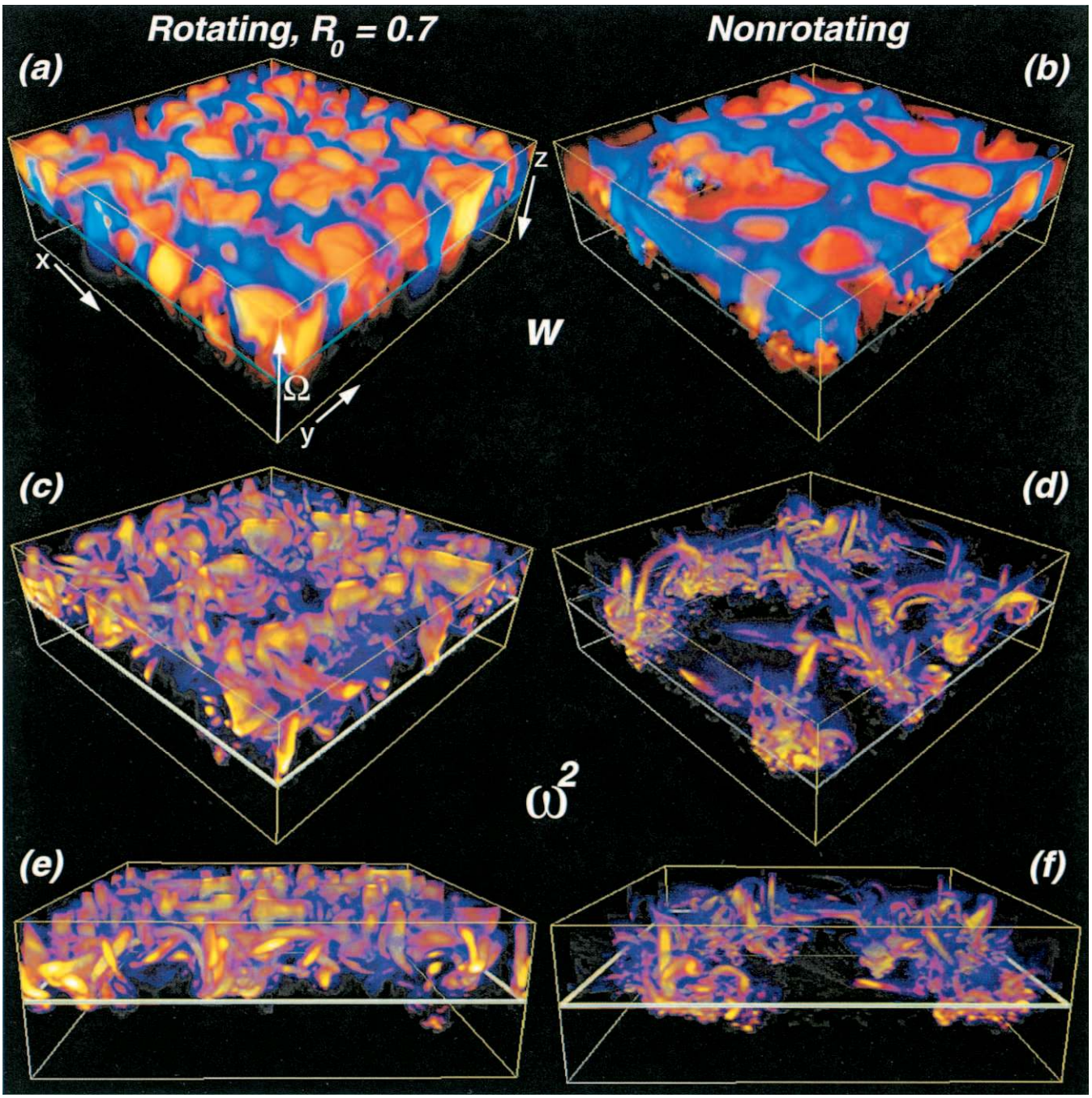

FIG. 17.—Comparison of rotating and nonrotating penetrative convection. Shown are volume renderings of (*a* and *b*) the vertical velocity w and (*c–f*) the enstrophy density ω^2 at a representative time for (*a*, *c*, and *e*) cases 10 and (*b*, *d*, and *f*) case 5. The rotation in case 10 is about the vertical axis parallel to gravity ($\phi = 90°$).

$\mathrm{Ro} = 0.7$. The figure shows volume renderings of vertical velocity from above (Figs. 17*a* and 17*d*) and enstrophy density from above (Figs. 17*b* and 17*e*) and the side (Figs. 17*c* and 17*f*) for both rotating and nonrotating cases. Some findings of the earlier nonpenetrative rotating work are apparent, and if anything, emphasized by the more disconnected nature of the penetrative topology. For example, the influence of rotation via the turning effect of the Coriolis force leads to generally smaller scales of motion in the flow. This is most noticeable in the upper cellular network of downflows in the first two companion figures (Figs. 17*a* and 17*d*); the granular cells of the rotating case are distinctly smaller. In the enstrophy density renderings (Figs. 17*b*, 17*c*, 17*e*, and 17*f*), this is manifested as a denser packing of the strong downflow structures, lending an overall impression of a greater degree of complexity in the rotating case. With the inclusion of significant rotational effects, the coherent plumes must all necessarily contain the same sense of vertical vorticity (positive or cyclonic), since they are "spun-up" as they are formed by convergent flows in the upper boundary layer. This property leads to greater interaction between plumes, since like-signed vorticity structures will tend to coalesce, and therefore creates stronger horizontal mixing while retarding the vertical mixing (Julien et al. 1996b; Brummell et al. 1996, 1998). This further adds to the increased complexity of the rotating flows and has important consequences for the penetration and overshooting that will be explained shortly.

Figure 18 exhibits snapshots of solutions where the Cartesian domain has been placed at various latitudes ($\phi = 45^\circ$, 15°, 0°) with all other parameters remaining fixed (cases 14, 12, and 11). The turbulent alignment of coherent structures that was discussed in detail in Brummell et al. (1996, 1998) is immediately apparent again in Figures 18*a*–18*d* in this penetrative companion to that work. The coherent, strong downflowing plume structures attempt to align themselves along the direction of the rotation vector. This effect, a natural result of the motion of fluid parcels subject to a rotational influence, is generally counteracted by two effects: the enforcement of vertical vorticity at the stress-free boundaries, and the desire of buoyancy to act in the direction of gravity. The former, and more artificial, of these constraints is less stringent in these penetrative cases than it was in the previous simulations (Brummell et al. 1996, 1998), since there is no stress-free boundary imposed at the base of the convecting domain. The alignment of the structures is allowed to continue into the stable layer, ceasing only when buoyancy braking effects decelerate the plume to a standstill. Hence, clear alignment can be seen over most of any coherent plume, with only a deviation toward vertical alignment near the upper boundary.

Figures 18*e*–18*h* exhibit renderings for $\phi = 0^\circ$, where the domain is positioned at the equator, and the rotation vector points along the y-axis. This configuration, in conjunction with the significant rotational influence provided at $\mathrm{Ro} = 1.0$, is quite constraining on the convective flows. As can be seen in the volume renderings of the vertical velocity in Figure 18*g*, the preferred mode is one where the three-dimensional cellular nature of the large-scale overturning is lost in favor of horizontal roll cells aligned in the y-direction. The figure shows turbulent, yet fairly clearly defined, north-south bands of upflow and downflow (*red and blue, respectively*) associated with these aligned rolls. The associated enstrophy density renderings (Figs. 18*e*, 18*f*, and 18*h*) show that the vortical nature of the turbulent solution is still apparent. Plume structures fill a significant fraction of the domain where the downflows of the quasi–two-dimensional rolls exist but are wrapped around the cells (in the east-west direction, x) by the strong, large-scale overturning of the rolls. At such low latitudes, the turbulent alignment mechanism is quenched, since it would require the contradictory phenomenon of horizontally flowing downflows. Combined with this, the presence of strong roll motions appears to overpower the coherent vortical structures, and so no clearly organized alignment of the plumes can be seen in Figure 18*f*.

4.2. *Dependence of Δ_p on Rotation Influence*

The two essential features of turbulent rotating convection identified above, i.e., the horizontal complexity induced by like-sign vortex interactions of the plumes and the alignment of plume structures with the rotation, are both likely to have significant consequences for the degree of overshooting. We quantify this by investigating four simulations carried out at different rotation rates, but with all other parameters held constant. We examine cases 5, 8, 9, and 10 that operate at $S = 7$, $\mathrm{Ra} = 5.5 \times 10^5$, $\mathrm{Pr} = 0.1$, and $\phi = 90^\circ$ and vary the Taylor number through $\mathrm{Ta} = (0,\ 5 \times 10^4,\ 5 \times 10^6,\ 1 \times 10^7)$, corresponding to convective Rossby numbers of $\mathrm{Ro} = (\infty,\ 10,\ 1,\ 0.71)$. Increasing the Taylor number while keeping the other parameters fixed does formally reduce the supercriticality of the solution, although these simulations are far from onset and so the incremental change is small. Furthermore, a posteriori measures of the degree of turbulence, such as the Reynolds numbers exhibited in Table 2, show that there are no order-of-magnitude changes that might influence the statistics of interest.

Figure 19 exhibits the resulting variation of the penetration depth Δ_p with the Rossby number, Ro. Clearly, Δ_p decreases with decreasing Ro, indicating that overshooting decreases with an increase in rotational influence. The points plotted indicate a relationship like $\Delta_p \sim \mathrm{Ro}^{0.15}$, although this is a best fit to only three points and is therefore untrustworthy. This decrease in the penetration is not immediately intuitive, since one might expect the coherent plumes in the presence of rotation to be more efficient at "drilling" into the stable zone with their increased vortical content drawn from the background rotation. On the contrary, however, the increased horizontal interaction (like-sign vortex mergers between the purely cyclonic plumes) brakes their vertical motion. Indeed, the rms velocities in the downflows of the $\mathrm{Ro} = 0.7$ case are only 60% of the strength of the nonrotating case, and this subsequently leads to a decrease in the overshooting depth.

The increased horizontal mixing does not enhance the overall thermodynamic homogenization of the interior, but rather reduces it, since this requires vertical mixing (see related discussions in Julien et al. 1996b for rotating Boussinesq convection and Brummell et al. 1996 for compressible nonpenetrative convection). Indeed, as can be seen in Figure 20, which exhibits the entropy gradient profiles for the simulations here, both the convective interior and the overshoot region become further removed from adiabatic as the rotation rate is increased. This reflects the well-known fact that fast-rotating systems tend to operate in a quasi–two-dimensional manner in a plane perpendicular to the rotation.

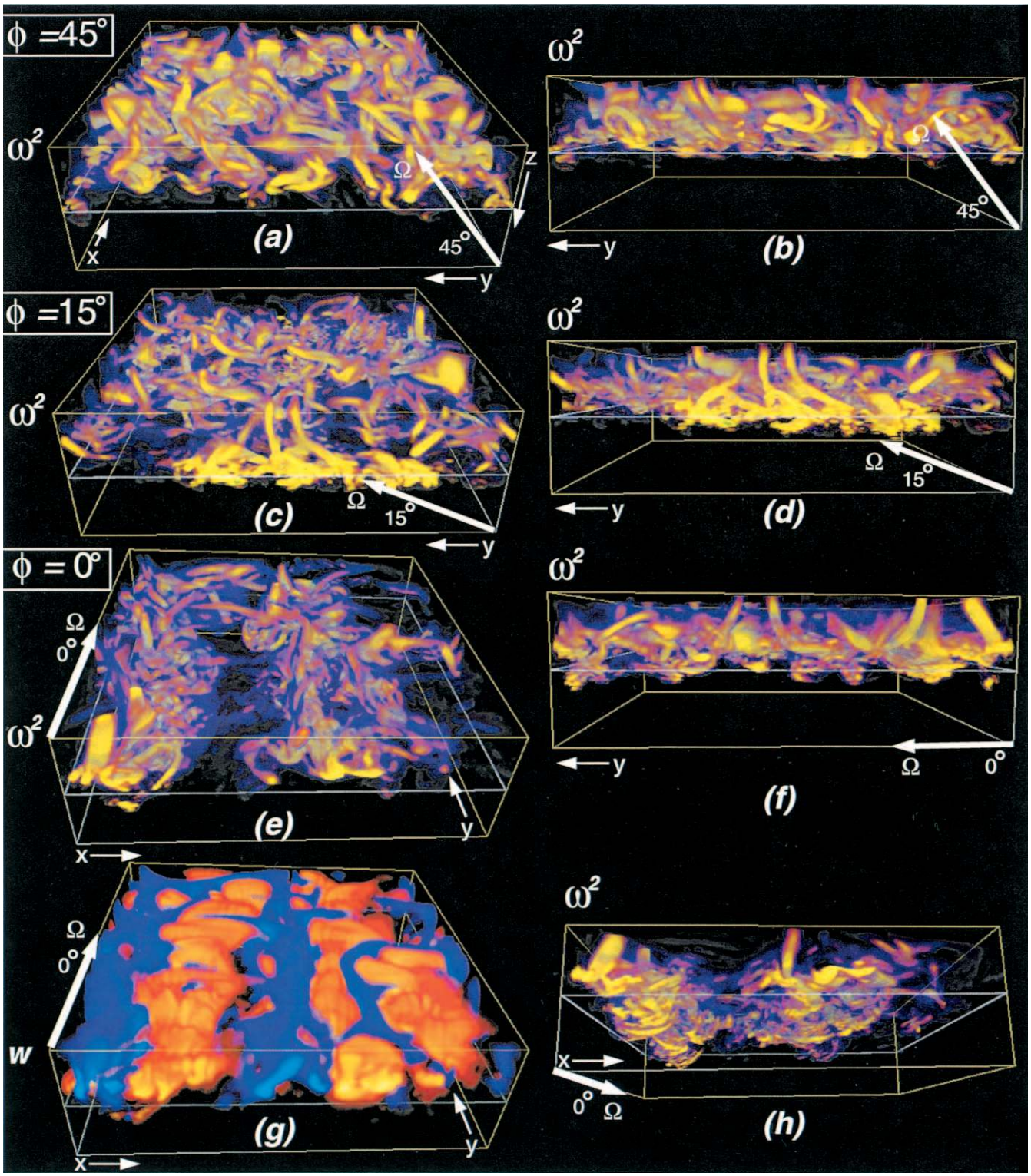

FIG. 18.—Penetrative convection with rotation at different latitudes. Shown are volume renderings of the enstrophy density ω^2 and the vertical velocity w at a representative time for (a, b) case 14 at latitude 45°, (c, d) case 12 at latitude 15°, and (e–h) case 11 at latitude 0°, the equator.

4.3. *Dependence of Δ_p on Latitude*

We investigate a series of simulations (cases 11–15 and case 9) where the latitudinal positioning of the f-plane model on the sphere is varied through $\phi = 0°$, 15°, 30°, 45°, 67°, and 90°, while the other parameters are kept fixed at $S = 7, \mathrm{Ra} = 5 \times 10^6, \mathrm{Pr} = 0.1,$ and $\mathrm{Ta} = 5 \times 10^6$ (corresponding to a convective $\mathrm{Ro} = 1.0$). Again, it should be noted that there are some consequences for the supercriticality of the flow, but these are minor. Figure 21 shows the values of Δ_p extracted from these calculations. The dependence of Δ_p on the latitude ϕ is not monotonic, but rather decreases from a maximum at $\phi = 90°$ to a minimum at $\phi \sim 30°$ and then recovers somewhat, increasing again at low latitudes ($\phi = 0°$, 15°). This dependence may be explained in terms of effects described previously. The high-

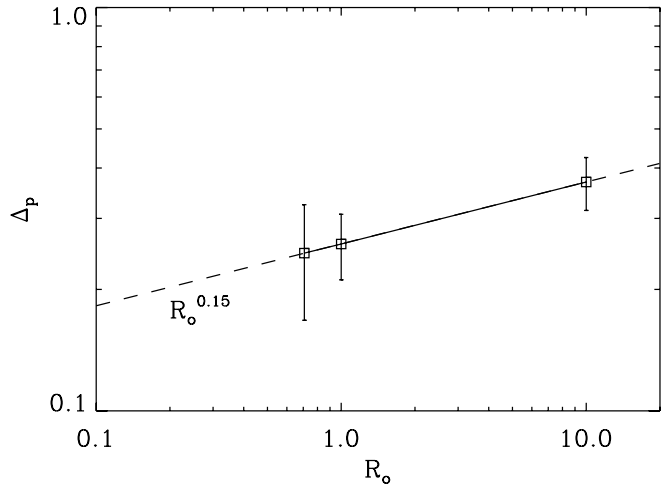

FIG. 19.—Penetration and overshooting measure Δ_p vs. Rossby number Ro. Shown are the results from cases 8, 9, and 10, where Ta varies such that the Rossby number Ro = 10, 1, 0.071 at $S = 7$ for the benchmark parameters at latitude $\phi = 90°$. A scaling line that fits the three points is added as a dashed line.

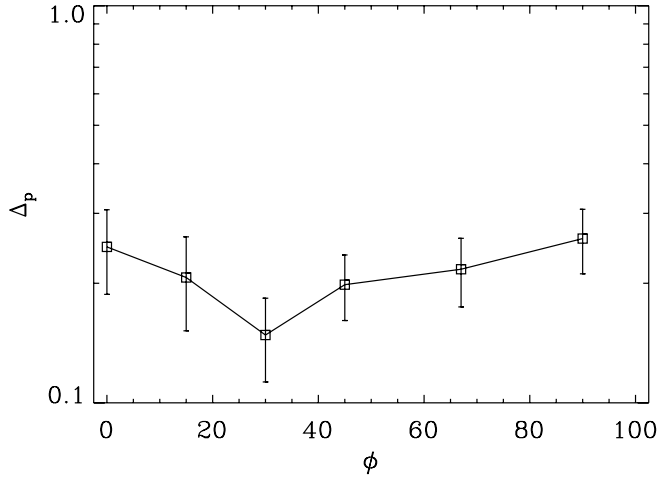

FIG. 21.—Variation of the penetration and overshooting measure Δ_p with latitude ϕ at $S = 7$ (cases 9, 15, 14, 13, 12, and 11). The latitude varies through $\phi = 90°$, 67°, 45°, 30°, 15°, and 0°.

latitude dependence may be attributed to the turbulent alignment of the plumes. Since the penetration is created by plumes piercing downward into the stable layer, then, away from the pole, the alignment of the plumes with the rotation vector means that they will be entering the stable region at an angle, rather than vertically. This angled penetration means that the buoyancy braking, which acts in the vertical direction, only has to counter the vertical component of the full plume velocity, and therefore we expect the penetration to be overcome at a shallower depth. This argument would imply that the penetration depth should decrease with decreasing latitude monotonically (between the pole and the equator) owing to the decreasing angle of incidence. However, this effect is mitigated at the lowest latitudes by the change in the topology of the convection demonstrated in Figures 18*e*–18*h*. The switch from a purely turbulent configuration, where the coherent plumes dominate the dynamics, to one that involves a large-scale quasi-laminar overturning roll motion, changes the penetration characteristics. The latter situation tends to have deeper penetration due to the larger filling factor of the motions below the interface and the enhanced Péclet numbers associated with flywheeling two-dimensional motions.

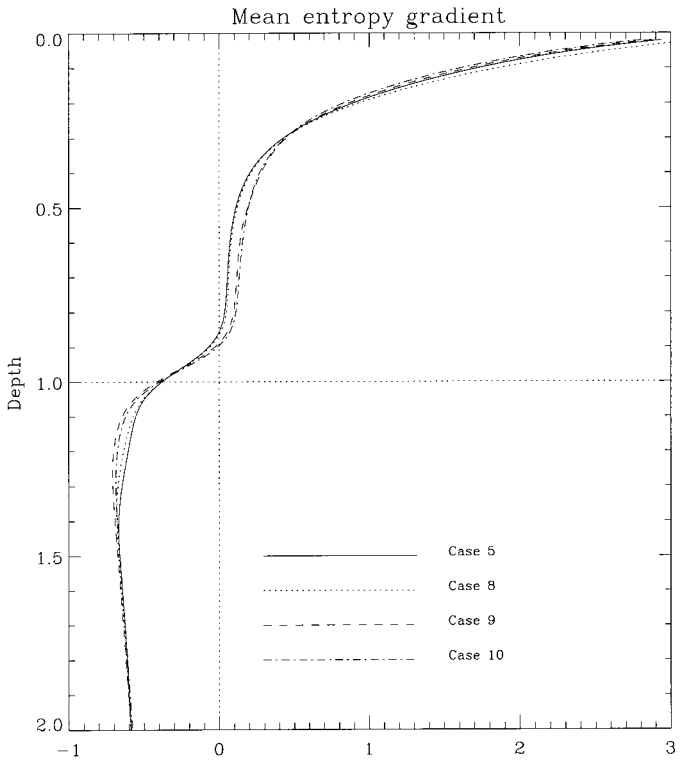

FIG. 20.—Time- and horizontally averaged entropy gradients for the cases with varying rotational influence at $S = 7$ (cases 5, 8, 9, and 10).

4.4. *Mean Flows*

We now address briefly the mean zonal $\langle u(z) \rangle$ and meridional $\langle v(z) \rangle$ flows that can exist when rotation is present. These mean flows may be generated by velocity correlations induced by the Coriolis force that lead to nonzero Reynolds stress source terms. In turbulent simulations such as these, the velocity correlations tend to be weak and are mainly associated with the turbulent alignment of the vortical downflows, as discussed in detail in Brummell et al. (1998). We present the mean flows found in these rotationally influenced simulations in Figure 22. There are no clear monotonic trends associated with either the increase in rotational influence (Figs. 22*a* and 22*b*) or the variation of latitude (Figs. 22*c* and 22*d*) in the mean zonal and meridional flows. This is likely due to the large fluctuations in the mean flows induced by inertial oscillations allowed in the *f*-plane model, even though these profiles are averaged over many (between 15 and 400) inertial time periods. The rms variations about these mean values can be on the order of 3 times the average value, and the maximum excursions can easily be twice that value again. Such large fluctuations make it very difficult to extract meaningful statistics about the mean flows. However, one significant conclusion may be drawn: a portion of each mean flow exists in the overshoot region that is as significant as those in the bulk of the convection zone. That is, these mean flows do not cut off at $z = 1$, but rather appear to continue to be generated at least down to the penetration depth. This result may be anticipated since we associate the

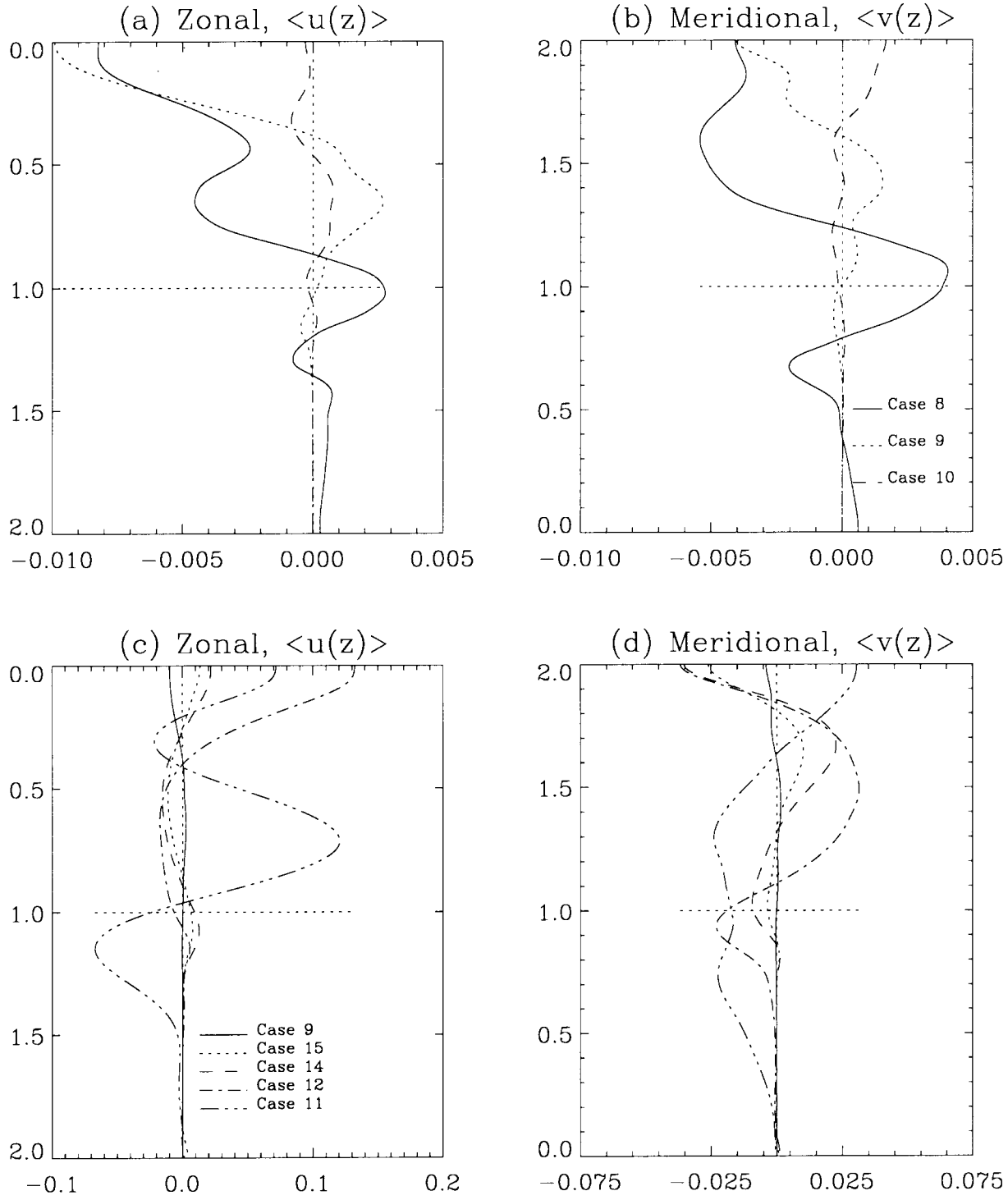

FIG. 22.—Mean zonal and meridional flows generated in rotating penetrative convection. The time- and horizontally veraged zonal $\langle u(z)\rangle$ and meridional $\langle v(z)\rangle$ flows are shown with (*a*, *b*) exhibiting the cases with varying rotational influence (cases 8, 9, and 10) and (*c*, *d*) displaying the cases with fixed rotational influence but varying latitude (cases 9, 15, 14, 12, and 11).

generation of these mean flows with velocity correlations built in the coherent downflows, and these are the very motions that overshoot into the stable region. This result implies that mean flows resulting from the dynamics of the convection zone may extend deeper than the convection zone itself (defined as the adiabatic region) even when no true penetration is found. Since the zonal flow is the analogue of the differential rotation under the local model approximation, this result should be borne in mind when interpreting the overlap of tachocline shear regions and the convection zone from helioseismic deductions.

5. DISCUSSION

We have described the results of a series of three-dimensional compressible convection simulations designed to examine the overshooting and penetration of highly turbulent convective motions from a convection zone into a stable

layer below. We have found that the coherent structures (or plumes) of the turbulent convection overshoot into the stable layer but do not thermodynamically mix efficiently enough to create an adiabatic zone that extends below the unstable-stable interface. This means that penetration in the technical sense is not occurring but rather the motions are overshooting. We ascribe this fact mainly to the small filling factor of the strong downflowing plumes that pierce into the stable zone. This lack of mixing to an adiabatic state occurs despite vigorous overshooting in the cases simulated. We find that, for the parameters studied here, average measures such as the penetration depth Δ_p exhibit a significant overshooting when compared to the local pressure scale height, H_p; for the range of simulations discussed, $0.4H_p \leq \Delta_p \leq 2H_p$. The variation of the relative stability of the lower layer, S, causes a significant variation in Δ_p. The penetration depth appears to follow the scaling $\Delta_p \sim S^{-1/4}$ approximately, in keeping with the theory presented in Hurlburt et al. (1994) for a thermal adjustment layer. A different scaling ($\Delta_p \sim S^{-1}$) was proposed in that paper for true penetration that extended the adiabatic region, but this has not found in these three-dimensional calculations for any of the parameters studied. In attempts to predict the behavior of more turbulent solutions, we anticipate that increasing the Péclet number by decreasing the thermal diffusivity offers the most likely path toward regaining true penetration, although no conclusive indications for its return have been found here.

The effect of rotation on the overshooting was also examined. We find that the inclusion of rotation decreases the penetration depth, and we attribute this to a braking of the vertical flows by the horizontal interactions induced between the like-sign vortical elements. Strong rotation leads to an alignment of the turbulent downflowing plumes with the rotation vector, so that, away from the poles, the structures attempt to penetrate the stable region at an angle rather than from vertically. This leads to a diminished degree of overshooting. Near the equator, the nearly horizontal rotation vector favors a convective topology that consists of quasi–two-dimensional rolls in the north-south direction that overpower the smaller scale turbulent vortical motions somewhat and destroy their turbulent alignment. This leads to an increased penetration depth compared to mid-latitudes due to the greater filling factor of the large-scale overturning motions and the enhanced Péclet number of the flywheeling quasi–two-dimensional motions.

A time series analysis of the penetration shows that distribution of penetration depths is skewed, with a tail incorporating some rare deeper events. It is interesting to speculate as to whether such unexpected deeper penetrative events could significantly affect the mixing and transport of passive or active ingredients, such as chemical species or magnetic fields.

We have conducted these simulations in the hope of gaining some insight into the dynamics of the lower solar convection zone and the tachocline. This region is thought to play an active role in the large-scale solar dynamo that produces the solar cycle of magnetic activity. The insights that we have sought are related to the fundamental physics of a convection zone interfacing to a stable region. We are unable to simulate this situation at realistic solar parameters since it is impossible with current resources to represent the range of turbulent scales present in the solar convection zone. We have however conducted our simulations at the highest degree of turbulence possible and have exhibited scaling laws for properties when possible. These scalings must be taken into account when applying our results to the Sun. For example, the significant degree of penetration that we find may be affected by the higher Péclet number, Reynolds number, and S, and the lower Prandtl number of the solar case. We may estimate the solar values from our current results, although such guesses will be highly conjectural since the behavior must be extrapolated over many orders of magnitude for some parameters. Proceeding with caution, if we extrapolate from our highest Péclet number ($\sim$1000) to an estimated solar value of $\mathrm{Pe} \sim 10^4$, the penetration fraction could be reduced by a factor of about 3. Using the estimated solar value for $\mathrm{Pr} \sim 10^{-8}$ would further reduce the value by a factor of 2 under the scalings that we have found. Estimating S for the Sun is a little more difficult, since S is based upon our original polytropic initial conditions, which of course do not exist for the solar case. We can however compare the superadiabatic gradient in the convection zone to the subadiabatic gradient in the overshoot region in the nonlinear state of both our model and a standard solar model (e.g., Christensen-Dalsgaard et al. 1996). The solar model would give a contrast in $\nabla - \nabla_{ad}$ of about 6 orders of magnitude (over a region from just below the bottom of the convection zone to within 10% of the top, covering the same density contrast as our models), whereas our models only show less than 2 orders of magnitude in this measure. However, the large value of $\nabla - \nabla_{ad}$ in the solar case is not necessarily all due to the stability ratio of the two layers, since the efficient convection at high Reynolds number in the convection zone will also contribute dramatically by reducing the superadiabatic gradient there without affecting the subadiabatic gradient below much at all. Proceeding for the sake of argument then with an increase in S by 2 orders of magnitude, say, Δ_p could be further reduced by a factor of 3 from our stiffest value. We can see that, by these extrapolations, the seemingly large degree of penetration encountered in these simulations (40%–$200\% \times H_p$) is quickly reduced to a range spanning 2%–11% of a pressure scale height. This range encompasses the latest helioseismic findings, such as the estimate of the penetration depth $\sim 0.07H_p$ quoted in Monteiro, Christensen-Dalsgaard, & Thompson (1994).

We do hope that some of the physical principals that we find are robust and shed light on solar phenomena. For example, how much the convection zone and tachocline interact is a question that is fundamental to an understanding of the dynamics of the layers and how they achieve their transport and mixing. Observationally, the existence of the tachocline is inferred from helioseismic inversions (Thompson et al. 1996) and shows up as a strong shear in the differential rotation profile (although unfortunately the helioseismic kernels cannot resolve the layer well). The characteristics of the convection zone, on the other hand, are normally predicted by numerical calculations of solar models. In these, the parameterized hydrostatic equations are fitted to observed quantities, including the luminosity, radius, and mass of the star, and the fractional abundances of hydrogen, helium, and heavy elements (for a review see Christensen-Dalsgaard et al. 1996). From such models, the base of the convection zone is then taken to be where the adiabatic region ends, and this is generally assumed to include an extension of the adiabatically mixed region due to penetrating convective motions (see, e.g., Christensen-

Dalsgaard et al. 1991; Kosovichev & Fedorova 1991). With the position and width of these two elements predicted by different means, it is not surprising that most current predictions for the internal structure of the Sun exhibit the convection zone and the tachocline as overlapping, with the degree of overlap varying with latitude. It has been tempting from the early simple models of penetration (Schmitt et al. 1984; Zahn 1991) to ascribe this overlap to true penetrative motions that extend the adiabatically mixed convection zone beyond the original interface into the stable tachocline region. In this paper, we have found that the highly turbulent three-dimensional convective motions overshoot significantly but do not exhibit this true penetration. The adiabatic region is not extended into the stable zone, but contrarily appears to shrink above the interface to accommodate the thermal adjustment region that characterizes the overshooting. We further note that even in the original simulations of Hurlburt et al. (1994), the nearly adiabatic region created by true penetration did not join *contiguously* with the adiabatic interior of the convection zone. The penetration zone was not a simple extension of the convection zone but had an interior adjustment region. It is possible that this lack of continuity is a result of the penetrative model that we have chosen, where the thermal conductivity is solely a function of depth. However, without actually performing the simulations, it is hard to predict if making the conductivity a function of temperature and density would significantly change the results, since the conductivity is then inextricably intertwined with the mean stratification. Preliminary analyses of a model employing a Kramer's law conductivity function (D. H. Porter & P. Woodward 2000, private communication) indicate that the mean temperature and density are not drastically altered. It would seem that none of the current models fit into the picture of an adiabatic convection zone smoothly extended into the stable region below to provide an overlap between the regions, as has been envisaged previously in standard solar modeling. One might argue again that our simulations are not performed at the solar parameters and more astrophysical values for the Péclet and Reynolds numbers may provide different results, for example, a greater degree of true adiabatic penetration. The trends exhibited in our simulation set appear not to concur with this hypothesis, although it is dangerous to extrapolate these results too far.

However, our simulations here suggest that overshooting motions do provide a physical interaction between the convectively unstable and stable regions. These motions appear to be strong, although of a low filling factor, and therefore may achieve significant vertical transport while not mixing well horizontally. These facts have significant consequences for chemical mixing, gravity wave generation, and magnetic field transport. For example, we anticipate that passive scalars may be mixed down to the overshoot depth. This result further bodes well for the solar magnetic activity cycle, since the overshooting is essential for transporting magnetic field from the convection zone into the strong shear of the tachocline, where amplification of the toroidal field may then take place. An efficient mechanism for transporting, or "pumping," the magnetic field out of the convection zone is shown to exist in papers related to this one (Tobias et al. 1998, 2001). The overshooting motions appear to provide the required dynamical connection between the convection zone and the tachocline. Since it is not provided by true penetrative motions, the observational overlap of shearing and adiabatic regions must stem from other processes. One possibility is that the mean flows induced at the base of the convection zone by the action of rotation on the overshooting coherent plumes create this effect.

The behavior of these three-dimensional simulations does also shed some light on certain helioseismic results. Investigations have deduced that there is no evidence for a sharp transition between the adiabatic zone and the radiative interior (Basu, Antia, & Narasimha 1994; Monteiro et al. 1994; Roxburgh & Vorontsov 1994). The smooth ramping of the entropy gradient over a deep thermal adjustment region, as exhibited in the high Pe simulations here, as opposed to a sudden transition from adiabatic to subadiabatic layers, may account for this result. The false expectation of such a sharp transition may affect the helioseismic predictions of the overshooting depth. Our simulations also exhibit a latitudinal dependence with a reduced overshooting depth at mid-latitudes that is consistent with an analysis of solar data by Monteiro & Thompson (1998). The investigations of that paper concerning the variation of the depth of the base of the convection zone with latitude revealed a sharper transition between the convection zone and the tachocline at mid-latitudes. In the light of our simulations, this could be associated with the narrower thermal adjustment region associated with the overshooting at mid-latitudes (although that paper interpreted the results in a different manner).

We would like to thank Douglas Gough and Jean-Paul Zahn for many useful discussions. This work was partially supported under NSF grant ESC-9217394 and NASA grants NAG 5-2256 and NCCS 5-151. The computations were performed initially on the IBM SP2 at the Cornell Theory Center, then subsequently on the Cray T3Es at the Pittsburgh and San Diego Supercomputing Centers and the Origin 2000 at the National Center for Supercomputing Applications.

REFERENCES

Adrian, R. J. 1975, J. Fluid Mech. 69, 753
Basu, S., Antia, H. M., & Narasimha, D. 1994, MNRAS, 267, 209
Bogdan, T. J., Cattaneo, F., & Malagoli, A. 1994, ApJ, 407, 316
Brandenburg, A., Nordlund, A., Pulkinnen, P., Stein, R. F., & Tuominin, I. 1990, A&A, 232, 277
Brummell, N. H., Hurlburt, N. E., & Toomre, J. 1996, ApJ, 473, 494
———. 1998, ApJ, 493, 955
Cattaneo, F., Brummell, N. H., Toomre, J., Malagoli, A., & Hurlburt, N. E. 1991, ApJ, 370, 282
Cattaneo, F., Hurlburt, N. E., & Toomre, J. 1989, in Stellar and Solar Granulation, ed. R. J. Rutten & G. Severino (Dordrecht: Kluwer), 415
———. 1990, ApJ, 349, L63
Chan, K. L., & Sofia, S. 1986, ApJ, 307, 222
———. 1987, Science, 235, 465
Christensen-Dalsgaard, J., Gough, D. O., & Thompson, J. 1991, ApJ, 378, 413
Christensen-Dalsgaard, J., et al. 1996, Science, 272, 1286
Deardorff, J. W., Willis, G. E., & Lilley, D. K. 1969, J. Fluid Mech., 35, 7
Edwards, J. M. 1990, MNRAS, 242, 224
Elliott, J., Miesch, M., & Toomre, J. 2000, ApJ, 533, 546
Furumoto, A., & Rooth, C. 1961, Geophysical Fluid Dynamics (Woods Hole: Oceanographic Inst. Rep.)
Gilman P. A. 1975, J. Atmos. Sci., 32, 1331
———. 1977, Geophys. Astrophys. Fluid Dyn., 8, 93
Gilman, P. A., & Dikpati, M. 2000, ApJ, 528, 552
Gilman, P. A., & Fox, P. A. 1997, ApJ, 484, 439
———. 1999, ApJ, 510, 1018
Gilman, P. A., & Miller, J. 1986, ApJS, 61, 585
Glatzmaier, G. A. 1984, J. Comput. Phys., 55, 461
———. 1985a, ApJ, 291, 300
———. 1985b, Geophys. Astrophys. Fluid Dyn., 31, 137
Glatzmaier, G. A., & Gilman, P. A. 1981a, ApJS, 45, 351

Glatzmaier, G. A., & Gilman, P. A. 1981b, ApJS, 47, 103
Goode, P. R., Dziembowski, W. A., Korzennik, S. G., & Rhodes, E. J. 1991, ApJ, 367, 649
———. 1977, in IAU Colloq. 38, Problems of Stellar Convection, ed. E. A. Spiegel & J.-P. Zahn (Berlin: Springer), 151
Gough, D. O. 1997, Nature, 388, 324
Gough, D. O., & MacIntyre, M. E. 1998, Nature, 394, 755
Graham, E. 1975, J. Fluid Mech., 70, 689
Hossain, M., & Mullan, D. J. 1990, ApJ, 354, L33
Hurlburt, N. E., Toomre J., & Massaguer, J. 1984, ApJ, 282, 563
———. 1986, ApJ, 311, 563
Hurlburt, N. E., Toomre, J., Massaguer, J. M., & Zahn, J.-P. 1994, ApJ, 421, 245
Jennings, R. L., Brandenburg, A., Nordlund, Å., & Stein, R. F. 1992, MNRAS, 259, 465
Julien, K., Legg, S., McWilliams, J., & Werne, J. 1996a, Dyn. Atmos. Oceans, 24, 237
———. 1996b, J. Fluid Mech., 322, 243
Kosovichev, A. G., & Fedorova, A. V. 1991, AZh, 68, 1015
Kuhfuss, R. 1986, A&A, 160, 116
Kumar, P., & Quataert, E. J. 1997, ApJ, 475, L143
Latour, J., Toomre, J., & Zahn, J.-P. 1981, ApJ, 311, 563
Malagoli, A., Cattaneo, F., & Brummell, N. H. 1990, ApJ, 361, L33
Malkus, W. V. R. 1960, Aerodynamic Phenomena in Stellar Atmospheres (Bologna: Zanichelli)
Massaguer, J., Latour, J., Toomre, J., & Zahn, J.-P. 1984, A&A, 140, 1
Massaguer, J., & Zahn, J.-P. 1980, A&A, 87, 315
Matthews, P. C. 1994, in ASP Conf. Ser. 68, Solar Active Region Evolution: Comparing Models with Observations, ed. K. S. Balasubramaniam & G. W. Simon (San Francisco: ASP), 56
Miesch, M., Elliott, J., Toomre, J., Clune, T., Glatzmaier, G., & Gilman, P. A. 2000, ApJ, 532, 593
Monteiro, M. J. P. F. G., Christensen-Dalsgaard, J., & Thompson, M. 1994, A&A, 283, 247
Monteiro, M. J. P. F. G., & Thompson, M. 1998, in Proc. of the SOHO6/GONG98 Workshop (ESA SP-418; Noordwijk: ESA), 819
Moore, D. R., & Weiss, N. O. 1973, J. Fluid Mech., 61, 553
Musman, S. 1968, J. Fluid Mech., 31, 343
Muthsam, H. J., Göb, W., Kupka, F., Liebich, W., & Zöchling, J. 1995, A&A, 293, 127
Myrup, L., Gross, D., Hoo, L. S., & Goddard, W. 1970, Weather, 25, 150
Nordlund, Å. 1982, A&A, 107, 1
———. 1983, in IAU Symp. 102, Solar and Stellar Magnetic Fields: Origins and Coronal Effects, ed. J. O. Stenflo (Dordrecht: Reidel), 79
———. 1984, in The Hydromagnetics of the Sun (ESA SP-220; Noordwijk: ESA), 37
———. 1985, in Theoretical Problems in High-Resolution Solar Physics, ed. H. U. Schmitt (Munich: Max-Plank-Institute für Astrophysik), 1
Nordlund, Å., Brandenburg, A., Jennings, R. L., Rieutord, M., Ruokalainen, J., Stein, R. F., & Tuominen, I. 1992, ApJ, 392, 647
Nordlund, Å., & Stein, R. F. 1990, Comput. Phys. Commun., 59, 119
———. 1991, Challenges to Theories of Moderate-Mass Stars, ed. D. O. Gough & J. Toomre (Berlin: Springer), 141
Porter, D. H., & Woodward, P. R. 1994, ApJS, 93, 309
Porter, D. H., Woodward, P. R., Yang, W., & Mei, Q. 1990, in Ann. NY Acad. Sci. 617, Nonlinear Astrophysical Fluid Dynamics (New York: New York Acad. Sci.), 234
Priest, E. R. 1982, Solar Magnetohydrodynamics (Dordrecht: Reidel)
Pulkinnen, P. Tuominen, I., Brandenburg, A., Nordlund, Å., & Stein, R. F. 1993, A&A, 267, 265
Rast, M. P., Nordlund, Å., Stein, R. F., & Toomre, J. 1993, ApJ, 408, L53
Rast M. P., & Toomre J. 1993a, ApJ, 419, 224
———. 1993b, ApJ, 419, 240
Renzini, A. 1987, A&A, 188, 49
Richard, D., & Zahn J.-P. 1999, A&A, 347, 734
Roxburgh, I. W., & Simmons, R. 1993, A&A, 277, 93
Roxburgh, I. W., & Vorontsov, S. V. 1994, MNRAS, 268, 880
Saikia, E., Singh, H. P., Chan, K. L., Roxburgh, I. W., & Srivastava, M. P. 2000, ApJ, 529, 402
Schmitt, J. H. H. M., Rosner, R., & Bohn, H. U. 1984, ApJ, 282, 316
Singh, H. P., Roxburgh, I. W., & Chan, K. L. 1994, A&A, 281, L73
———. 1995, A&A, 295, 703
———. 1996, Bull. Astron. Soc. India, 24, 281
———. 1998a, in ASP Conf. Ser. 138, Proc. 1997 Pacific Rim Conf. on Stellar Astrophysics, ed. K. L. Chan, K. S. Cheng, & H. P. Singh (San Francisco: ASP), 313
———. 1998b, A&A, 340, 178
Sofia, S., & Chan, K. L. 1984, ApJ, 282, 550
Sparrow, E. M., Goldstein, R. J., & Jonsson, V. K. 1963, J. Fluid Mech., 18, 513
Spiegel, E. A. 1972, Physics of the Solar System, ed. S. I. Rasool (Washington DC: NASA)
Spiegel, E. A., & Zahn, J.-P. 1992, A&A, 265, 106
Stein, R., & Nordlund, Å. 1989, ApJ, 342, L95
———. 1991, in Challenges to Theories of Moderate-Mass Stars, ed. D. O. Gough & J.Toomre (Berlin: Springer), 195
———. 1994, in IAU Symp. 154, Infrared Solar Physics, ed. D. Rabin, J. Jeffries & C. Lindsey (Dordrecht: Kluwer), 225
Stein, R., Nordlund, Å., & Kuhn, J. R. 1989, in Stellar and Solar Granulation, ed. R. J. Rutten, & G. Severino (Dordrecht: Kluwer), 381
Thompson, M. J., & the GONG Dynamics Inversion Team, 1996, Science, 272, 1300
Tobias, S. M., Brummell, N. H., Clune, T. L., & Toomre, J. 1998, ApJ, 502, L177
———. 2001, ApJ, 549, 1183
Toomre, J., & Brummell, N. H. 1995, in Proc. 4th *SOHO* Workshop Helioseismology (ESA SP-376; Noorwijk: ESA), 47
Toomre, J., Brummell, N. H., Cattaneo, F., & Hurlburt, N. E. 1990, Comput. Phys. Commun., 59, 105
Toomre, J., Gough, D. O., & Spiegel, E. A. 1977, J. Fluid Mech., 79, 1
———. 1982, J. Fluid Mech., 125, 99
Townsend, A. A. 1964, Q. J. R. Meterol. Soc., 90, 248
van Ballegooijen, A. A. 1982, A&A, 113, 99
Veronis, G. 1963, ApJ, 137, 641
Watson, M. 1981, Geophys. Astrophys. Fluid Dyn., 16, 285
Weiss, N. O. 1994, in Lectures on Solar and Planetary Dynamos, ed. M. R. E. Proctor & A. D. Gilbert (Cambridge: Cambridge Univ. Press), 59
Weiss, N. O., Brownjohn, D. P., Matthews, P. C., & Proctor, M. R. E. 1996, MNRAS, 283, 1153
Xiong, D. R. 1985, A&A, 150, 133
Zahn, J.-P. 1991, A&A, 252, 179
Zahn, J.-P., Talon, S., & Matais, J. 1997, A&A, 322, 320
Zahn, J.-P., Toomre, J & Latour, J. 1982, Geophys. Astrophys. Fluid Dyn., 22, 159